

Development of a Reduced-Order Model for Hydrodynamic Analysis of a Wind-Assisted Ship

Downloaded from: https://research.chalmers.se, 2026-11-05 00:28 UTC

Citation for the original published paper (version of record):

Bakari, A., Alves Lopes, R., Eslamdoost, A. (2026). Development of a Reduced-Order Model for Hydrodynamic Analysis of a Wind-Assisted Ship. Journal of Sailing Technology, 11(1): 322 -347. http://dx.doi.org/10.5957/jst/2026.11.1.322

N.B. When citing this work, cite the original published paper.

research.chalmers.se offers the possibility of retrieving research publications produced at Chalmers University of Technology. It covers all kind of research output: articles, dissertations, conference papers, reports etc. since 2004. research.chalmers.se is administrated and maintained by Chalmers Library

(article starts on next page)

Journal of Sailing Technology 2026, volume 11, issue 1, pp. 322 - 347.
The Society of Naval Architects and Marine Engineers.

Development of a Reduced-Order Model for Hydrodynamic Analysis of a Wind-Assisted Ship

Abdoul-Malik Bakari
Chalmers University of Technology, Sweden, bakari@chalmers.se.

Rui Lopes
Chalmers University of Technology, Sweden.

Alex Abolfazl Shiri
RISE-SSPA Maritime Center, Sweden.

Arash Eslamdoost
Chalmers University of Technology, Sweden.

Manuscript received May 5, 2026; revision received August 13, 2026; accepted August 27, 2026.

Abstract. Decarbonization is one of the most pressing challenges facing the modern shipping industry. Wind-assisted ship propulsion (WASP) offers a promising pathway by integrating wind technologies with conventional systems, but understanding the hydrodynamic behaviour of such vessels under realistic conditions is essential for design optimisation. This study investigates the nominal wake field of a bare hull across various leeway angles and Froude numbers, along with pressure and wall shear stress distributions of a self-propelled ship under different leeway angles and reduced propeller thrust conditions. Computational Fluid Dynamics (CFD) simulations are performed for leeway angles from −9° to 9° and sail thrust values from 0% to 50% of ship resistance. A virtual disk model represents propeller effects under self-propulsion conditions. The CFD results are used to develop a Reduced-Order Model (ROM) combining Weighted Proper Orthogonal Decomposition (WPOD) and the Kriging method. This hybrid framework enables efficient flow field reconstruction across varying leeway angles, Froude numbers, and sail thrust values. Once trained, the ROM predicts wake fields, pressure, and shear stress within seconds, providing a fast alternative to high-fidelity CFD. Results show the ROM effectively captures the target field quantities while significantly reducing computational cost. The WPOD models achieve high accuracy, with average errors of 2.41% for mean wake fraction, 3.5% for resistance, and 3% for side force compared to reference CFD results.

Keywords: wind-assisted ship hydrodynamics; leeway angle; reduced-order method (ROM); proper orthogonal decomposition (POD).

NOMENCLATURE

A_0	Propeller disc area [m^2]
A_E	Propeller expanded blade area [m^2]
A_i	Projected cell face area in the x-direction [m^2]
A_j	Projected cell face area in the y-direction [m^2]
a_{ij}	Modal coefficient corresponding to the i-th snapshot and j-th POD mode [-]
B	Breadth [m]
$\mathbf{C}$	Modal coefficient matrix
C_{P}	Pressure coefficient [-]
C_{r}	Total resistance coefficient [-]

Downloaded from onepetro.org/JST/article-pdf/11/01/322/5433561/sname-jst-2026-15.pdf/1 by guest on 03 November 2026

C_{rf}	Frictional resistance coefficient [-]
C_{rp}	Pressure resistance coefficient [-]
C_{S}	Total side force coefficient [-]
C_{Sf}	Frictional side force coefficient [-]
C_{Sp}	Pressure side force coefficient [-]
C_τ	Skin-friction coefficient [-]
$\mathbf{c}_i$	Coefficient vector associated with the i-th snapshot
D_H	Propeller hub diameter [m]
D_P	Propeller diameter [m]
d_i	Distance vector between the i-th training sample and the test sample in parameter space
E_{total}	Total energy captured by POD modes [-]
F_n	Froude number [-]
J	Advance coefficient [-]
K_{Q}	Torque coefficient [-]
K_{T}	Thrust coefficient [-]
k	Number of retained POD modes [-]
L_{PP}	Length between perpendiculars [m]
ℓ_d	Dimension-specific correlation length scale
m	Number of flow solutions (snapshots) [-]
n	Number of spatial points [-]
P	Pressure [Pa]
P_P	Mean propeller pitch [m]
P_{w}	Wind thrust percentage [%]
p	Dimension of the parameter space [-]
R_{A}	Towing force [N]
R_{SF0}	Self-propulsion resistance at zero drift [N]
$\mathbf{S}$	Covariance matrix of the multivariate Gaussian distribution
S_{w}	Wetted surface area [m^2]
T_{AP}	Draught at aft perpendicular [m]
T_{FP}	Draught at fore perpendicular [m]
T_{M}	Draught at midship [m]
T_{W}	Wind thrust [N]
$\mathbf{U}$	Matrix of left singular vectors
$\mathbf{V}$	Matrix of right singular vectors
V_{s}	Ship speed [m s^{-1}]
V_x	Local axial velocity at the propeller plane [m s^{-1}]
w_i	Weight for the i-th training sample
w_{n}	Nominal wake fraction [-]
$\mathbf{X}$	Snapshot matrix
x_i	i-th snapshot
y^+	Dimensionless wall distance [-]
$z(x)$	Stochastic process with zero mean
$\boldsymbol{\alpha}$	Vector of regression coefficients [-]
β	Drift (leeway) angle [°]
ε_i	ROM error when the i-th snapshot is used as the test set in LOO cross-validation
$\varepsilon_{\mathrm{mean}}$	Mean ROM error
η	Energy threshold [-]
η_0	Open-water efficiency [-]
ρ	Water density [kg m^{-3}]
$\mathbf{\Sigma}$	Diagonal matrix containing the singular values
σ^2	Overall variance parameter

Downloaded from onepetro.org/JST/article-pdf/11/01/322/5433561/sname-jst-2026-15.pdf/1 by guest on 03 November 2026

σ_j	j-th singular value
τ	Wall shear stress [Pa]
$\mathbf{\Phi}_k$	Matrix containing the first k POD modes
ϕ_j	j-th POD mode
∇	Displaced volume [m^3]

3D	Three-dimensional
ARD	Automatic Relevance Determination
C3SE	Chalmers Centre for Computational Science and Engineering
CCM	Computational Continuum Mechanics
CFD	Computational Fluid Dynamics
IMO	International Maritime Organization
ITTC	International Towing Tank Conference
KLT	Karhunen–Loève Transform
LOO	Leave-one-out cross-validation
NAISS	National Academic Infrastructure for Supercomputing in Sweden
PCA	Principal Component Analysis
POD	Proper Orthogonal Decomposition
RANS	Reynolds-Averaged Navier–Stokes
RBF	Radial Basis Function
ROM	Reduced-Order Model
SIMPLE	Semi-Implicit Method for Pressure-Linked Equations
SST	Shear Stress Transport
STAR	Simulation of Turbulent Flow in Arbitrary Regions
SVD	Singular Value Decomposition
WASP	Wind-Assisted Ship Propulsion
WPOD	Weighted Proper Orthogonal Decomposition

1 INTRODUCTION

Decarbonization has become one of the most pressing challenges facing the Maritime Industry. Increasingly stringent environmental regulations and the global commitment to reduce greenhouse gas emissions have accelerated the development of alternative propulsion technologies. Among these, WASP has re-emerged as an economically attractive solution according to the International Maritime Organization (IMO, 2023). WASP can significantly reduce engine load and fuel consumption, thereby contributing directly to emission reduction targets (Khan et al., 2021). The investigations of Lu and Ringsberg (2020) and Ammar and Seddiek (2022) have demonstrated substantial reductions in fuel consumption, with reported savings ranging from 5.6% to 30%. In addition, CO_2 emissions can also be reduced by up to 30%, as reported by Lindstad et al. (2022).

WASP offers promising solutions for reducing emissions; however, it also introduces significant technical challenges. When wind-generated thrust is applied to a vessel, aerodynamic side forces induce leeway and heel (Clayton, 1987). These effects can change the propeller wake field and increase sail-induced resistance, as recently quantified for a tanker hull form (Bickert et al., 2026). Van Der Kolk et al. (2020) and Van Der Kolk et al. (2019) employed a RANS-based Computational Fluid Dynamics (CFD) approach to evaluate the performance of a wind-assisted ship under various leeway angles. The numerical results were validated against towing tank experiments. Simulations were conducted for both bare-hull and appended-hull configurations to analyze resistance, side force, and yaw moment. To analyze both hydrodynamic and aerodynamic effects, Sauder and Alterskjær (2022) conducted an empirical investigation of sail-assisted ships using a cyber–physical approach. The wind loads were modeled numerically, while the hydrodynamic parameters were experimentally eval-

Downloaded from onepetro.org/JST/article-pdf/11/01/322/5433561/sname-jst-2026-15.pdf/1 by guest on 03 November 2026

uated to assess propulsion performance. This integrated methodology provides a solid foundation for understanding the interaction between aerodynamic forces and ship hydrodynamics in wind-assisted propulsion systems. However, wind shear effects, sail-hull interaction, and detailed hydrodynamic flow behavior were not considered. The numerical investigation conducted by Saydam et al. (2022) examined the bare hull to assess the influence of leeway and heel angles. The results indicate that heel angles below 10° have a limited effect on resistance and side force. In contrast, an increase in leeway angle has a pronounced impact on the hydrodynamic behavior of the hull Bickert et al. (2026).

Despite CFD being a tool for high-fidelity analysis of WASP ship hydrodynamics, particularly for self-propulsion and wake field investigations, it is computationally expensive. Systematic parametric studies involving multiple leeway angles and propulsion conditions require a large number of simulations, resulting in high computational cost. To overcome this limitation, Reduced-Order Models (ROMs) based on Proper Orthogonal Decomposition (POD) have become a widely used method across different CFD fields for predicting flow fields. POD enables the extraction of dominant flow structures from high-dimensional datasets, providing a compact representation of the governing flow dynamics. For example, Tang et al. (2025) used the POD method to rapidly and efficiently predict the three-dimensional (3D) fluid flow and temperature fields in data centers. The computational time required by the POD-based reduced-order model is approximately one thousandth of that of the full CFD model. The work of Huayamave et al. (2017) demonstrated that POD reinforced with radial basis function (RBF) interpolation can accurately predict 3D CFD solutions. The proposed POD network was validated, showing that large-scale CFD problems can be effectively parameterized and significantly simplified within this framework.

Accurate POD-based predictions typically require a sufficiently large dataset to reconstruct the flow field reliably, which normally means running a large number of simulations to cover the parameter space in this case, the variation in leeway angle and Froude number, or, for the self-propulsion case, the variation in sail thrust. It would still be desirable to have accurate predictions using only a small number of simulation data points. To achieve this with a limited number of simulations, non-intrusive reduced-order modeling techniques that couple POD with interpolation or regression methods offer a promising approach. The Kriging method and interpolation techniques such as Radial Basis Functions (RBF) have been successfully combined with POD to construct non-intrusive reduced-order models capable of predicting flow fields at untrained parameter points. The hybrid POD-RBF framework allows rapid reconstruction of complex wake structures without solving the full Navier–Stokes equations, significantly reducing computational effort while maintaining acceptable accuracy. Bakari, A. Malik et al. (2025) employed the POD–RBF method to predict the wake field at the propeller plane for different drift angles, achieving an average prediction error of 7.5%. Xia and Wu (2025) proposed a hybrid reduced-order method that combines Weighted Proper Orthogonal Decomposition (WPOD) with Kriging interpolation. The efficacy of the WPOD-Kriging method was validated through three parametric CFD simulations, demonstrating its capability to handle multiple input parameters. With multiple parameters the WPOD method, combined with Kriging, can efficiently account for their combined effects and improve prediction accuracy for WASP. This approach significantly reduces the number of required high-fidelity CFD simulations across different parameters.

The objective of this paper is to develop and assess a ROM framework for predicting the hydrodynamic performance of a wind-assisted ship, enabling rapid estimation of flow-field quantities and hydrodynamic coefficients at operating conditions beyond those included in the CFD database. The investigated quantities are obtained across a range of leeway angles (−9° to 9°) and Froude numbers. Additionally, pressure and wall shear stress distributions are examined for a self-propelled WASP under different leeway angles and sail thrust (0% to 50%).

Downloaded from onepetro.org/JST/article-pdf/11/01/322/5433561/sname-jst-2026-15.pdf/1 by guest on 03 November 2026

2 METHODOLOGY

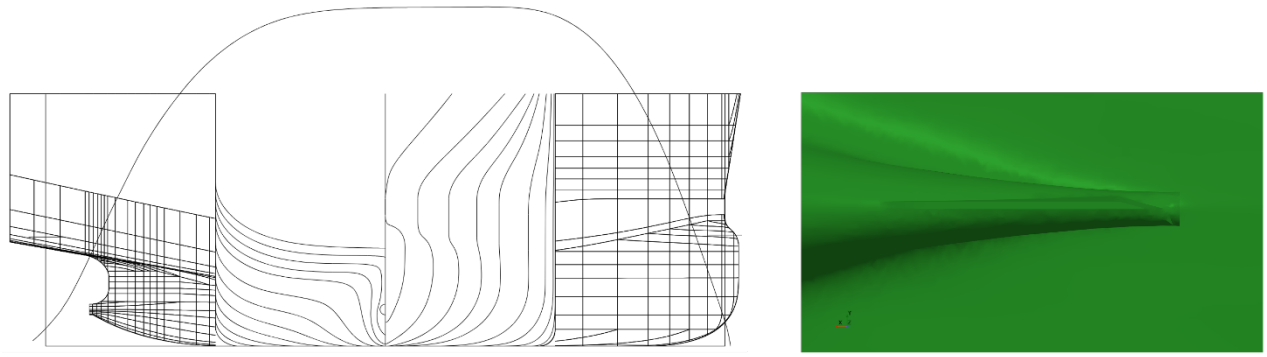
This section presents the CFD-based numerical methodology and the POD approach used to investigate the wake fraction for a bare hull and the pressure and wall shear stress distributions under various self-propulsion conditions. The first part describes ship geometry, the computational domain, boundary conditions, and mesh generation. The numerical setup for the bare-hull simulations performed at different drift angles and Froude numbers is described in detail. In addition, the definition of different sail thrust conditions for the self-propulsion methodology at a selected Froude number is explained. The second part presents the implementation of the WPOD model. It outlines the database construction used for construction and validation, including the selection of drift angles, Froude numbers, and operating conditions. Throughout this study, the leeway angle is taken as equivalent to the drift angle, and denoted by β.

2.1 CFD Numerical Method

The test case used in this study is the JoRes1 single-screw tanker (JoRes Project, 2023). The main particulars of the ship are presented in Table 1. The JoRes tanker shown in Figure 1 has a Length between perpendiculars (L_{PP}) of 178.5 m at full scale and 6.86 m at model scale. It should be noted that the hull has an asymmetric skeg to improve the wake that enters the propeller. The propeller of this ship has four blades, and its details are presented in Table 2. This study focuses only on the model scale. The open-water characteristics used to define the virtual disk model are obtained from the experimental model tests conducted by HSVA (2023). These tests provide the thrust coefficient (K_{T}), torque coefficient (K_{Q}), and open-water efficiency (η_0) as functions of the advance coefficient (J), as shown in Figure 2.

Table 1. Full-scale and model-scale particulars of JoRes1 tanker.

Parameter	Full scale	Model scale
Length between perpendiculars L_{PP} (m)	178.50	6.86
Breadth B (m)	32.26	1.24
Draught at fore perpendicular T_{FP} (m)	10.56	0.406
Draught at aft perpendicular T_{AP} (m)	10.38	0.399
Draught at midship T_{M} (m)	10.47	0.402
Wetted surface area S_{w} (m^2)	8337.10	12.68
Displaced volume ∇ (m^3)	46648	2.86



a) Lines plan and curve of sectional areas

b) Asymmetry part (Skeg) of the geometry

Figure 1. JoRes1 Geometry: a) lines plan and curve of sectional areas; b) asymmetry part (skeg) of the geometry.

Downloaded from onepetro.org/JST/article-pdf/11/01/322/5433561/sname-jst-2026-15.pdf/1 by guest on 03 November 2026

Table 2. Main particulars of propeller.

Parameter	Full Scale	Model Scale
Diameter, D_P (m)	6.50	0.250
Mean pitch ratio, P_P/D_P	0.790	0.790
Hub diameter ratio, D_H/D_P	0.140	0.140
Disc area ratio, A_E/A_0	0.449	0.449
Number of blades	4	4

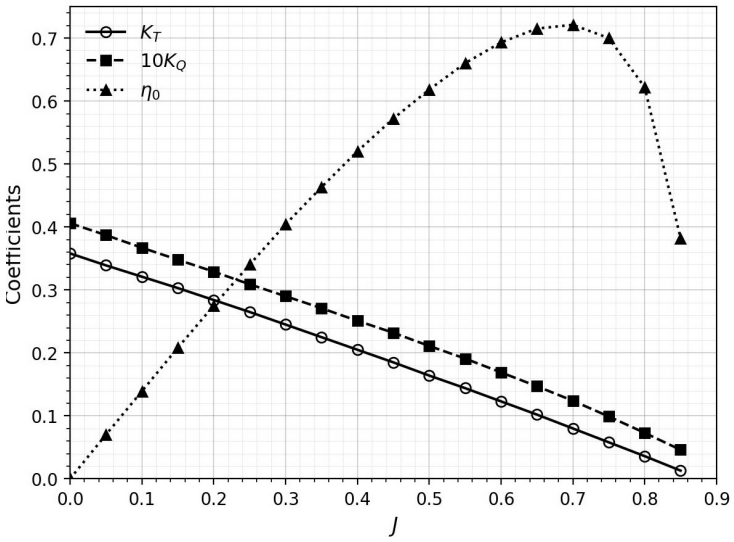


Figure 2. Open water curve of the JoRes 1 tanker propeller.

All CFD simulations in this study were carried out using Simcenter STAR-CCM+ (version 2024.10.1). The flow is assumed to be incompressible and Newtonian. The Reynolds-Averaged Navier-Stokes (RANS) equations are solved using a finite-volume method for simulations. To reduce computational cost, free-surface effects are neglected, and a double-body approach is adopted. This assumption is commonly applied in resistance and propulsion studies and provides reliable results for the present analysis, as reported by Larsson et al. (2013) and Jiang et al. (2022). Pressure-velocity coupling is handled by a segregated solver using the SIMPLE algorithm. All simulations are performed in steady state for the bare hull and unsteady for the self-propulsion case with a fixed time step of 0.01 s. A wall-resolved approach is ensured by keeping the target y^+ below 1 on the hull surface. The simulations are computed using the k–ω SST turbulence model in accordance with ITTC (2011) recommendations. The water density ρ is set to 999 kg m^{-3}.

Two types of simulations are conducted in this study. First, bare-hull simulations are performed for various drift angles and Froude numbers. From these computations, the axial velocity distribution at the propeller plane is extracted to evaluate the nominal wake fraction. The nominal wake fraction w_n is defined as

$$w_n = 1 - \frac{V_x}{V_\mathrm{s}}, \tag{1}$$

where V_x is the local axial velocity at the propeller plane and V_s is the ship advance speed. The studied drift angles range between −9° and 9°, and the Froude numbers range from 0.137 to 0.182. The CFD wake fields are extracted and used to build the POD model. Second, self-propulsion simulations are performed at a single Froude number (0.162). For this condition, various propeller loadings are

Downloaded from onepetro.org/JST/article-pdf/11/01/322/5433561/sname-jst-2026-15.pdf/1 by guest on 03 November 2026

considered corresponding to the wind thrust. The resistance obtained at self-propulsion for a drift angle of 0° with a 0% sail thrust case, R_{SF0}, is used as a reference to estimate wind thrust. The target wind thrust is defined as:

$$T_{\mathrm{W}} = P_w \left(R_{\mathrm{SF0}} - R_{\mathrm{A}} \right), \tag{2}$$

where R_{A} is the towing force for compensating for the Reynolds number difference between model scale and full scale, and P_w is the percentage of thrust coming from the wind sails.

Following the ITTC guidelines (ITTC, 2011), the computational domain is established as a rectangular region with a total length of $6L_{\mathrm{PP}}$. The distance from the inlet to the hull is $2L_{\mathrm{PP}}$ and $3L_{\mathrm{PP}}$ from the transom to the outlet. The lateral and bottom boundaries are positioned at a distance of $2L_{\mathrm{PP}}$ from the ship. The top boundary is located at the design draft level. Appropriate inlet, outlet, symmetry, and wall boundary conditions are applied accordingly, as shown in Figure 3.

The computational mesh consists of unstructured, trimmed hexahedral cells with local refinements in regions of high flow gradients, particularly around the hull and in the propeller region for self-propulsion cases. Prism layers are generated along the hull surface to accurately resolve the boundary layer. All meshes are generated using the automatic meshing tool in STAR-CCM+. Figure 4 illustrates the discretization of the computational domain. The total number of cells used in the present study is approximately 5 million. Numerical uncertainty defines an interval expected to contain the exact (true) solution. It is evaluated following the procedure proposed by Eça and Hoekstra (2014), which provides a systematic framework for estimating discretization errors and assessing simulation accuracy. In the unstructured grid topology, exact geometric similarity between grid levels cannot be strictly achieved; however, the grid refinement parameters are kept as consistent as possible to ensure a reliable estimate of uncertainty. The numerical uncertainty analysis for the present configuration and operating conditions has been previously conducted in Bakari, A. Malik et al. (2026). The overall numerical uncertainty is reported to be below 18%.

2.2 POD Method

POD, also known as the Karhunen-Loève Transform (KLT) or Principal Component Analysis (PCA), is a widely employed projection-based model-order reduction technique in the CFD field (Giere, 2016). The goal of POD is to extract dominant modes from high-fidelity datasets, which can then be used to reconstruct the original field with reduced computational cost. This subsection presents a comprehensive examination of the mathematical foundations, numerical implementation, and practical considerations associated with POD-based reduced-order modeling in wake, pressure, and wall shear stress prediction.

2.2.1 POD Fundamentals

Consider a collection of m flow solutions (e.g., axial velocity, pressure, or wall shear stress), each representing a time average of a flow field. These realizations, commonly referred to as snapshots, contain flow field information at n spatial points. The snapshot matrix is constructed as:

$$\mathbf{X} = [\mathbf{x}_1, \mathbf{x}_2, \cdots, \mathbf{x}_m \,] \in R^{n \times m}, \tag{3}$$

where each column vector $\mathbf{x}_i$ represents a single snapshot. A crucial preprocessing step involves the removal of the temporal mean from each snapshot to ensure statistical stationarity:

$$\langle \mathbf{x}_i \rangle = 0, \quad \forall i \in \{1, \ldots, m\}. \tag{4}$$

Downloaded from onepetro.org/JST/article-pdf/11/01/322/5433561/sname-jst-2026-15.pdf/1 by guest on 03 November 2026

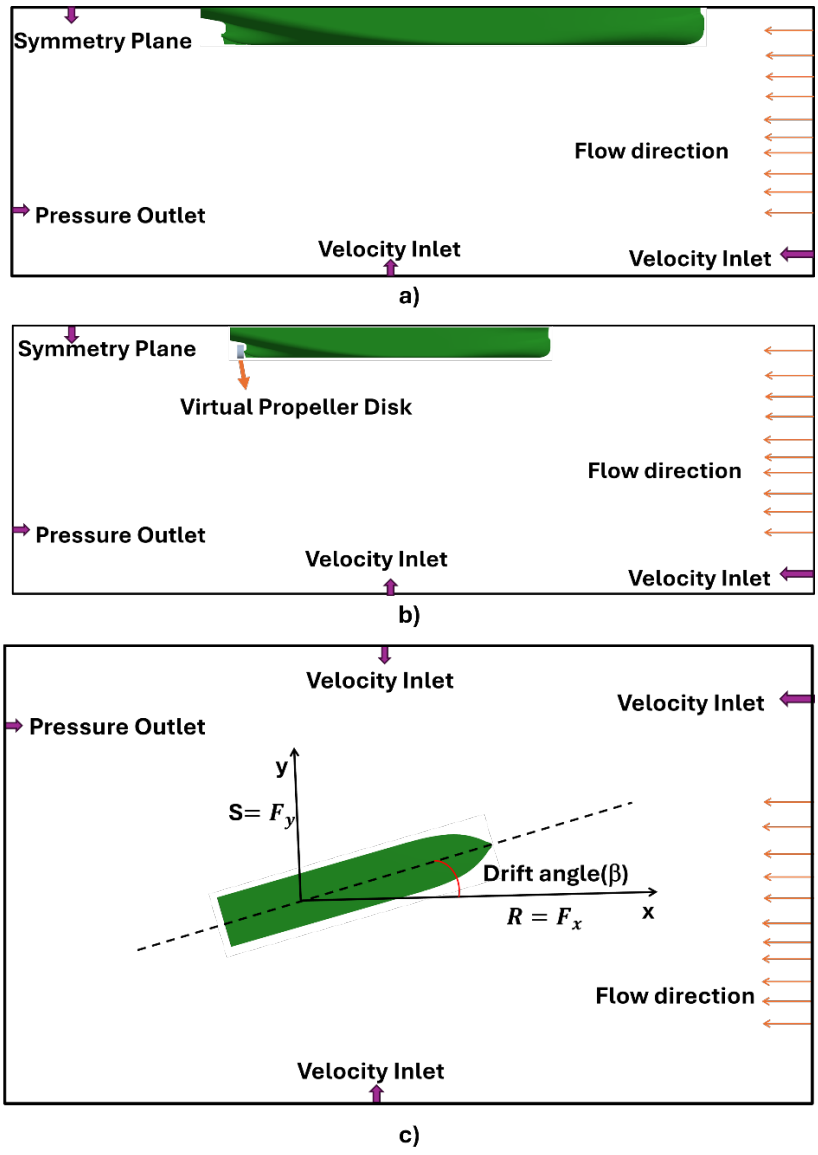


Figure 3. Flow direction and boundary condition setup for the CFD simulations: (a) bare hull boundary conditions; (b) self-propulsion boundary conditions; (c) boundary condition definition and flow direction.

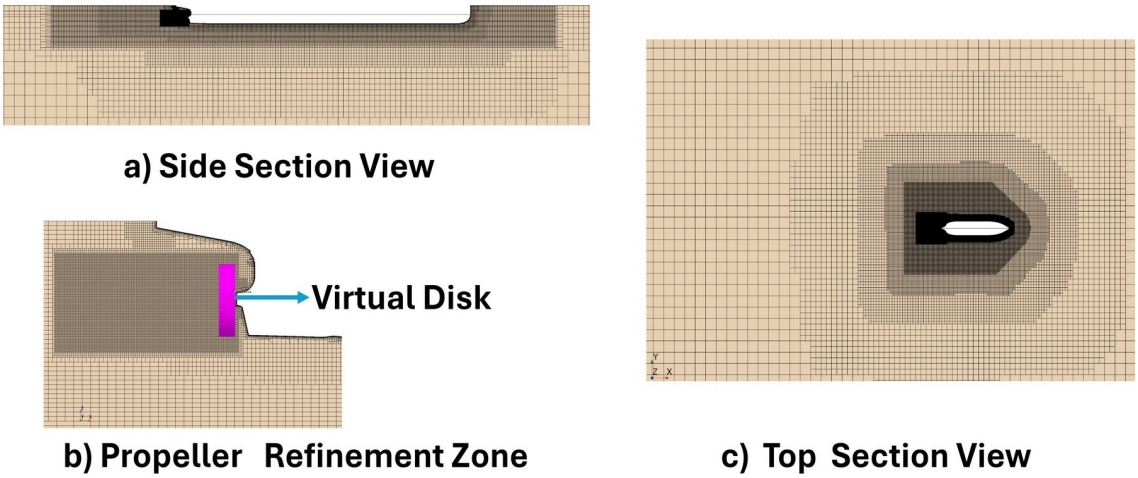


Figure 4. Mesh details: (a) side section view; (b) propeller refinement zone; (c) top section view.

Downloaded from onepetro.org/JST/article-pdf/11/01/322/5433561/sname-jst-2026-15.pdf/1 by guest on 03 November 2026

This mean subtraction ensures that the subsequent decomposition captures the fluctuating components of the flow, which are typically of primary interest in dynamic analysis. The POD framework represents each snapshot through a linear combination of reduced-order basis vectors expressed as:

$$\mathbf{x}_i = \sum_{j=1}^{m} a_{ij} \boldsymbol{\phi}_j, \tag{5}$$

where $\boldsymbol{\phi}_j \in \mathbb{R}^n$ represents the j-th POD mode and a_{ij} denotes the corresponding modal coefficient for the i-th snapshot. The mathematical framework is elaborated by Giere (2016). The most numerically robust and computationally efficient approach to computing POD modes is via the Singular Value Decomposition (SVD). The snapshot matrix is decomposed as:

$$\mathbf{X} = \mathbf{U}\boldsymbol{\Sigma}\mathbf{V}^T = \mathbf{U}\left(\boldsymbol{\Sigma}\mathbf{V}^T\right). \tag{6}$$

The SVD equation has three key matrices. The matrix $\mathbf{U}$ contains the left singular vectors, which are precisely the POD modes $\boldsymbol{\phi}_j$. The matrix $\boldsymbol{\Sigma} \in \mathbb{R}^{n\times m}$ is a diagonal matrix holding the singular values $\sigma_1 > \sigma_2 > \cdots > \sigma_m$. Finally, $\mathbf{V} \in \mathbb{R}^{m\times m}$ is the matrix of right singular vectors.

The singular values σ_j quantify the energy contribution of each corresponding mode, with the total energy of the system given by:

$$E_{\text{total}} = \sum_{j=1}^{m} \sigma_j^2 \,, \tag{7}$$

where σ_j^2 represents the energy captured by the j-th mode. The coefficient matrix $\mathbf{C} = \boldsymbol{\Sigma}\mathbf{V}^T \in \mathbb{R}^{m\times m}$ stores the modal coefficients. Each column $\mathbf{c}_i = [a_{i1}, a_{i2}, \ldots, a_{im}]^T$ contains the coefficients for the i-th snapshot.

A fundamental aspect of POD-based ROM is truncating the modal basis to retain only the most energetic structures. This truncation dramatically reduces the system's dimensionality while preserving its essential physics. The cumulative energy criterion determines the number of retained modes k such that:

$$\frac{\sum_{i=1}^{k} \lambda_i}{\sum_{i=1}^{m} \lambda_i} \geq \eta, \tag{8}$$

where η represents the energy threshold, selected as 0.99, and λ_i are singular values. This criterion ensures that the reduced basis captures the predominant dynamics while filtering out low-energy noise or insignificant flow features. With the truncated POD basis $\boldsymbol{\Phi}_k = [\boldsymbol{\phi}_1, \boldsymbol{\phi}_2, \ldots, \boldsymbol{\phi}_k] \in \mathbb{R}^{n\times k}$ and corresponding coefficient vectors $\mathbf{a}_i = [a_{i1}, a_{i2}, \ldots, a_{ik}]^T$, any snapshot can be approximated as:

$$\mathbf{x}_i \approx \sum_{j=1}^{k} a_{ij} \boldsymbol{\phi}_j = \boldsymbol{\Phi}_k \mathbf{a}_i, \tag{9}$$

This approximation achieves optimality in the sense that it minimizes the reconstruction error for any given basis size k, a property that follows directly from the Eckart-Young theorem as explained by Kolda (2003).

Downloaded from onepetro.org/JST/article-pdf/11/01/322/5433561/sname-jst-2026-15.pdf/1 by guest on 03 November 2026

2.2.2 Kriging Method

After obtaining the POD basis, we need to establish the relationship between the input parameters of our problem (i.e., drift angle β, Froude number F_n, or wind thrust T_{W}) and the reduced basis coefficients. Predicting coefficients for new parameter combinations can be formulated as an interpolation problem in the parameter space. Kriging provides an effective nonlinear interpolation framework for this purpose. The method combines a regression model with a stochastic process, as explained by Mohammadi and Raisee (2019). The regression component can take various forms, including constant, linear, or polynomial models. In this work, we adopt the linear regression model. The stochastic component offers several correlation-function options, including linear, Gaussian, and spherical models. Here, we employ the Gaussian correlation model. The Kriging predictor is expressed as:

$$y(\mathbf{x}) = \mathbf{f}(\mathbf{x})^T \boldsymbol{\alpha} + z(\mathbf{x}), \tag{10}$$

where $\mathbf{f}\,(\mathbf{x})^T$ contains the basis functions of the regression model, $\boldsymbol{\alpha}$ is the vector of regression coefficients, and $z(x)$ denotes a stochastic process with zero mean:

$$\mathbb{E}\left[z(x)\right] = 0. \tag{11}$$

This formulation allows us to generate POD coefficients for any parameter, enabling rapid flow-field prediction across the parameter space of interest.

2.2.3 WPOD-Kriging Method

Xia and Wu (2025) proposed a hybrid reduced-order method that combines weighted proper orthogonal decomposition with Kriging. The approach assigns appropriate weights to samples when estimating specific design parameters, with the main innovation being an optimized method for generating these weights. The weight generation process employs a leave-one-out strategy. For each iteration, the samples are divided into a training set and a test set. The Euclidean distance between the training set and test set in the parameter space is converted into weights using a multivariate Gaussian distribution. The weight for the the i-th training sample is computed as:

$$w_i = \frac{1}{(2\pi)^{p/2}|\mathbf{S}|^{1/2}} \exp\left(-\frac{1}{2} d_i^T \mathbf{S}^{-1} d_i\right), \tag{12}$$

where d_i is the vector of distances between the the i-th training sample and the test sample in the parameter space, p is the dimension of the parameter space, and S is the covariance matrix of the multivariate Gaussian distribution. Using these weights, the WPOD-Kriging method constructs a reduced-order model from the training set and compares its predictions against the test set to obtain the error. By repeatedly cycling through different training and test set configurations, multiple errors are generated and averaged to calculate a global error. The covariance matrix can then be optimized by minimizing this global error:

$$\varepsilon_{\mathrm{mean}} = \frac{1}{m} \sum_{i=1}^{m} \varepsilon_i, \tag{13}$$

where the summation $\sum_{i=1}^{m}$ is taken over all snapshots from $i = 1$ to m, and ε_i is the individual error of the ROM when the i-th snapshot is used as the test set in the leave-one-out cross-validation (LOO) method. The optimization seeks the covariance matrix Σ that minimizes this mean error, thereby identifying the optimal weight distribution for the parameter space. This weighted formulation enhances local predictive accuracy while maintaining the computational efficiency of projection-based reduced-order modeling. This optimization achieves an optimal weight-generation strategy.

Downloaded from onepetro.org/JST/article-pdf/11/01/322/5433561/sname-jst-2026-15.pdf/1 by guest on 03 November 2026

2.2.4 Automatic Relevance Determination for Anisotropic Parameter Spaces

The WPOD-Kriging framework employs Automatic Relevance Determination (ARD) to handle anisotropic correlations in the multi-dimensional parameter space. Unlike isotropic kernels that assume uniform correlation length across all input dimensions, ARD assigns independent length-scale parameters to each input dimension, enabling the model to automatically identify the relative importance of different parameters (Ortali et al., 2021). The ARD Gaussian correlation function is expressed as:

$$k(\mathbf{x}, \mathbf{x}') = \sigma^2 \exp\left(-\frac{1}{2} \sum_{d=1}^{p} \frac{(x_d - x'_d)^2}{\ell_d^2} \right), \tag{14}$$

where σ^2 represents the overall variance parameter, p denotes the dimensionality of the parameter space, and ℓ_d are the dimension-specific length-scale parameters. Each ℓ_d controls the correlation length along its corresponding input dimension, with larger values indicating slower variation (i.e., the output is less sensitive to changes in that parameter), while smaller values indicate rapid variation and thus higher relevance. Using an ARD kernel allows the surrogate model to automatically weight the influence of different design parameters (such as the drift angle and the Froude number) based on their actual impact on the flow field, rather than treating them as equally important.

3 RESULTS

This section presents the application of the WPOD reduced-order model to predict the nominal wake field at the propeller plane, the pressure distribution over the hull surface, and the wall shear stress distribution along the hull. The model was built in Python. The predictions are compared against reference CFD results for various operating conditions, including different drift angles, Froude numbers, and propeller loading conditions corresponding to different sail thrusts. From these predicted fields, the mean wake fraction, resistance, and side force coefficients are derived and compared against the CFD target data.

3.1 The Model Prediction

In this study, POD is used to predict different quantities. The first part (Case 1) involves predicting the nominal wake field for different Froude numbers F_n and drift angles β for the bare hull simulations. The second part (Case 2) focuses on predicting the pressure and wall shear stress distributions around the hull for various wind thrust values T_{W} and drift angles β, with a fixed Froude number. Table 3 summarizes the data used to build the model for both cases.

The model is constructed based on three Froude numbers or wind thrust values across a range of drift angles and subsequently predicts at intermediate Froude numbers or wind thrust values for selected drift angles. All models are constructed on an Intel Core i9-14900 system.

3.2 Nominal Wake Prediction

The design of a ship propeller requires a careful analysis of the axial velocity field at the propeller plane. A detailed understanding of this flow field is essential because it directly influences the inflow conditions experienced by the propeller. An accurate characterization of the axial velocity distribution allows the designer to improve propeller performance, efficiency, and cavitation behaviour. One of the key parameters describing the inflow condition is the wake fraction. The wake fraction represents the reduction of the inflow velocity at the propeller plane compared with the free-stream ship speed. It quantifies the velocity deficit generated by the hull boundary layer and the viscous wake that develops along the stern. The wake fraction is defined in Equation 1.

Downloaded from onepetro.org/JST/article-pdf/11/01/322/5433561/sname-jst-2026-15.pdf/1 by guest on 03 November 2026

Table 3. Data used to build the model and prediction parameters for both case studies.

Case	Parameter	Data used for WPOD	Prediction data	Fixed
Case 1: Wake Field	F_n	0.137, 0.162, 0.182	0.137, 0.149, 0.162, 0.172, 0.182	–
	β (°)	–9, –8, –6, –4, –2, 0, 2, 4, 6, 8, 9	–9, –8, –7, –6, –5, –4, –3, –2, 0, 2, 3, 4, 5, 6, 7, 8, 9	–
Case 2: Pressure/Shear	T_{W} (%)	0, 30, 50	0 to 50	F_n = 0.162
	β (°)	–9, –8, –6, –4, –2, 0, 2, 4, 6, 8, 9	–9, –8, –7, –6, –5, –4, –3, –2, 0, 2, 3, 4, 5, 6, 7, 8, 9	F_n = 0.162

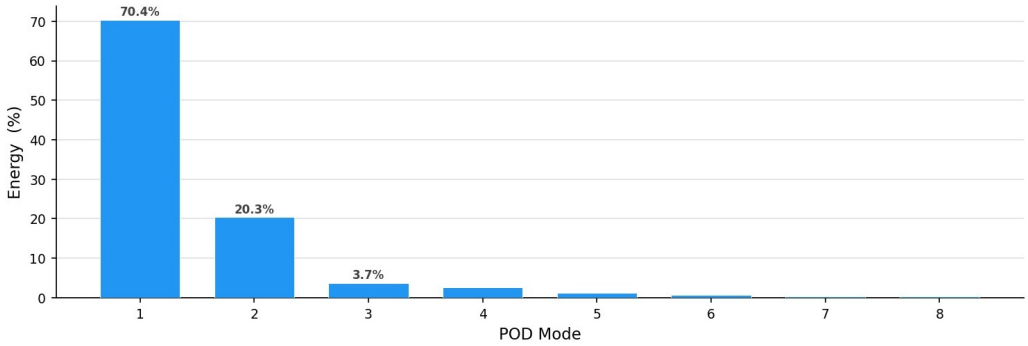


Figure 5. POD mode analysis: energy distribution.

For WASP, the inflow conditions at the propeller plane differ significantly from those of conventional vessels. The aerodynamic thrust generated by the sails modifies the force balance on the vessel and changes the operating point of the propulsion system. In addition, the presence of leeway introduces asymmetric flow conditions around the hull. Variations in the leeway angle alter the wake field behind the stern, leading to substantial changes in the axial velocity distribution at the propeller plane. As a result, the wake fraction is no longer constant and may vary with both the leeway angle and the wind-induced thrust forces. Therefore, predicting the wake field accurately under these conditions becomes particularly important for the proper design and operation of the propeller. In this section, the WPOD method is employed to reconstruct and predict the axial velocity field at the propeller plane for different drift and sail thrust conditions.

The WPOD model was constructed to predict the wake field at the propeller plane. A total of eight modes were retained in the reduced-order model, which allows the reconstruction to reach a theoretical accuracy of approximately 99.9% based on the cumulative energy content of the POD modes. Once the dominant modes are identified, the optimal covariance matrix is obtained through the WPOD formulation. The construction of the WPOD model is computationally efficient, requiring a few seconds, which is negligible for practical applications. This rapid model generation highlights the advantage of reduced-order modelling techniques for analysing complex flow fields obtained from CFD simulations. Figure 5 shows the energy distribution of the POD modes. It can be observed that the first four modes already capture more than 98% of the total energy contained in the POD snapshots. This indicates that the dominant flow structures in the wake field can be accurately represented using only a small number of modes, while the remaining modes contribute mainly to small-scale corrections.

Figure 6 and Figure 7 show the wake fields at drift angles β = 0° and β = 7°, respectively, at F_n = 0.149. These cases were not included in the dataset used to construct the model. Each figure presents the wake field obtained from the CFD simulation and the wake field predicted by the WPOD

Downloaded from onepetro.org/JST/article-pdf/11/01/322/5433561/sname-jst-2026-15.pdf/1 by guest on 03 November 2026

model, and the difference between the two fields in the rightmost plot. The results show only a very small difference between the CFD and WPOD predictions. The local difference between the two fields remains around 0.1, indicating that the error is generally below 10%. The prediction at the larger drift angle appears to be slightly more accurate than at β = 0°. This may be explained by the stronger wake disturbances at higher drift angles, which allow more coherent flow structures to be captured by the decomposition. At β = 0°, most of the velocity field is close to zero, resulting in fewer dominant structures to extract.

For the Froude number F_n = 0.172, which was not used for construction of the model, Figure 8 and Figure 9 present the comparison of the wake fields for drift angles β = 0° and β = −8°, respectively. The comparison shows that the main differences between the CFD and POD predictions occur primarily in regions with low wake values. In this case, the maximum local difference percentage error remains below 15% relative to the CFD results. However, the average difference error between the two fields remains below 6%, indicating good overall agreement between the CFD simulations and the WPOD predictions.

The wake field analysis is important for propeller design, particularly for evaluating the mean wake fraction. Figure 10 shows the nominal mean wake obtained from the CFD simulations and the values predicted by the WPOD model. As observed, the predicted mean wake follows a similar trend to the CFD results, with only small differences appearing at higher drift angles. The smallest Froude number, F_n = 0.137, presents the highest mean wake for both the CFD and the model predictions. This indicates that the wake field is more disturbed at lower Froude numbers.

For most drift angles, the model slightly underpredicts the mean wake compared with the CFD values. However, the difference remains very small, with an average error of 2.41% for all F_n and β. This small discrepancy indicates that the WPOD model can predict the mean wake with acceptable accuracy. This model provides fast, accurate predictions of the wake field, allowing rapid estimation of the flow characteristics for different operating conditions.

3.3 Pressure Prediction

Under different sail thrust conditions, the propeller suction effect in the aft region of the hull can alter the pressure distribution. Both the propeller unloading and the leeway (drift) angle can therefore modify the pressure distribution along the hull surface. Changes in these parameters may alter the hydrodynamic forces acting on the vessel, particularly at the aft. This subsection focuses on predicting the pressure distribution over the hull and evaluating the integrated pressure force coefficients from the predicted pressure field.

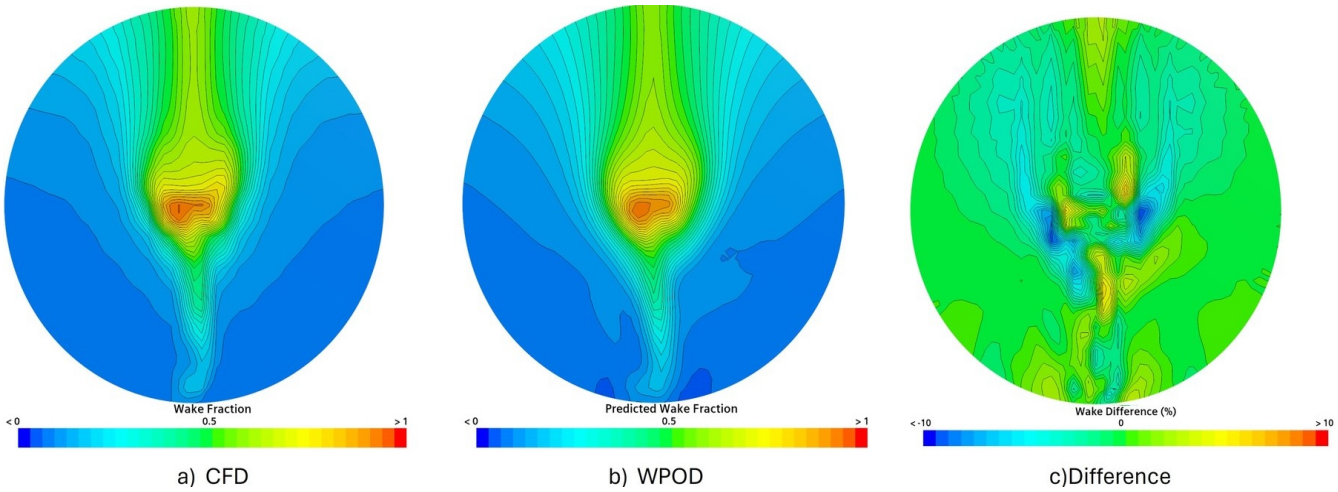


Figure 6. Wake prediction at F_n = 0.149 and drift angle β = 0°: (a) CFD; (b) WPOD; (c) Difference.

Downloaded from onepetro.org/JST/article-pdf/11/01/322/5433561/sname-jst-2026-15.pdf/1 by guest on 03 November 2026

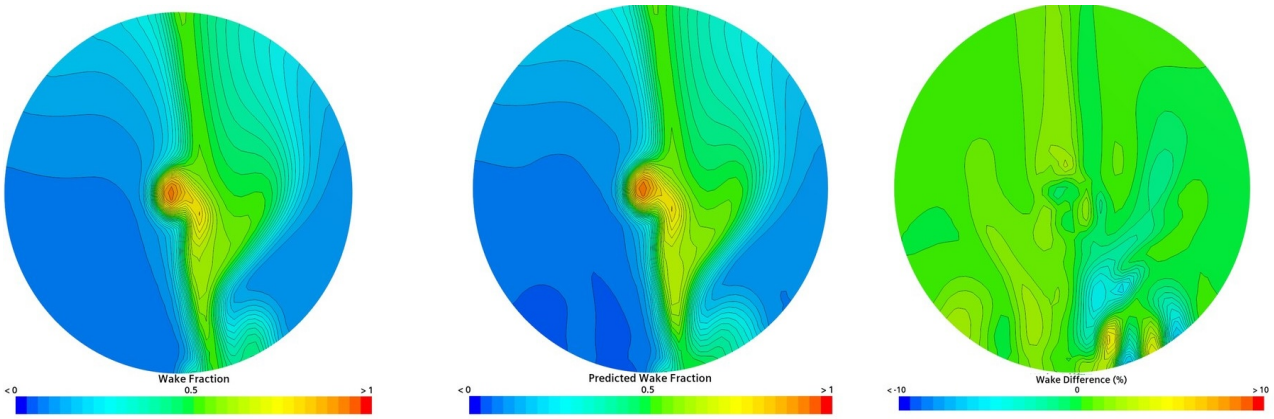


Figure 7. Wake prediction at F_n = 0.149 and drift angle β = 7°: (a) CFD; (b) WPOD; (c) Difference.

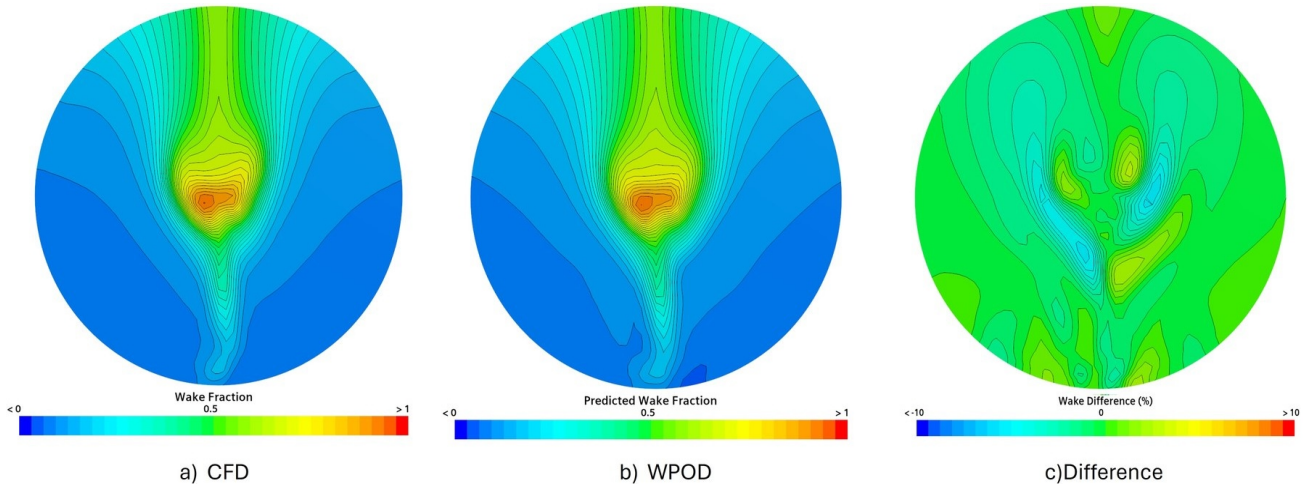


Figure 8. Wake prediction at F_n = 0.172 and drift angle β = 0°: (a) CFD; (b) WPOD; (c) Difference.

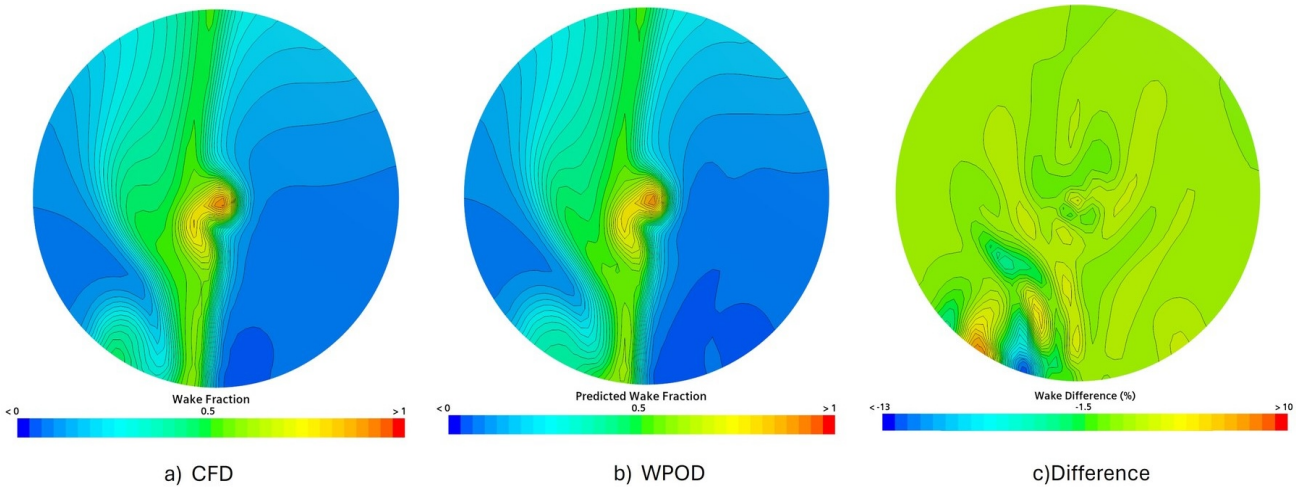
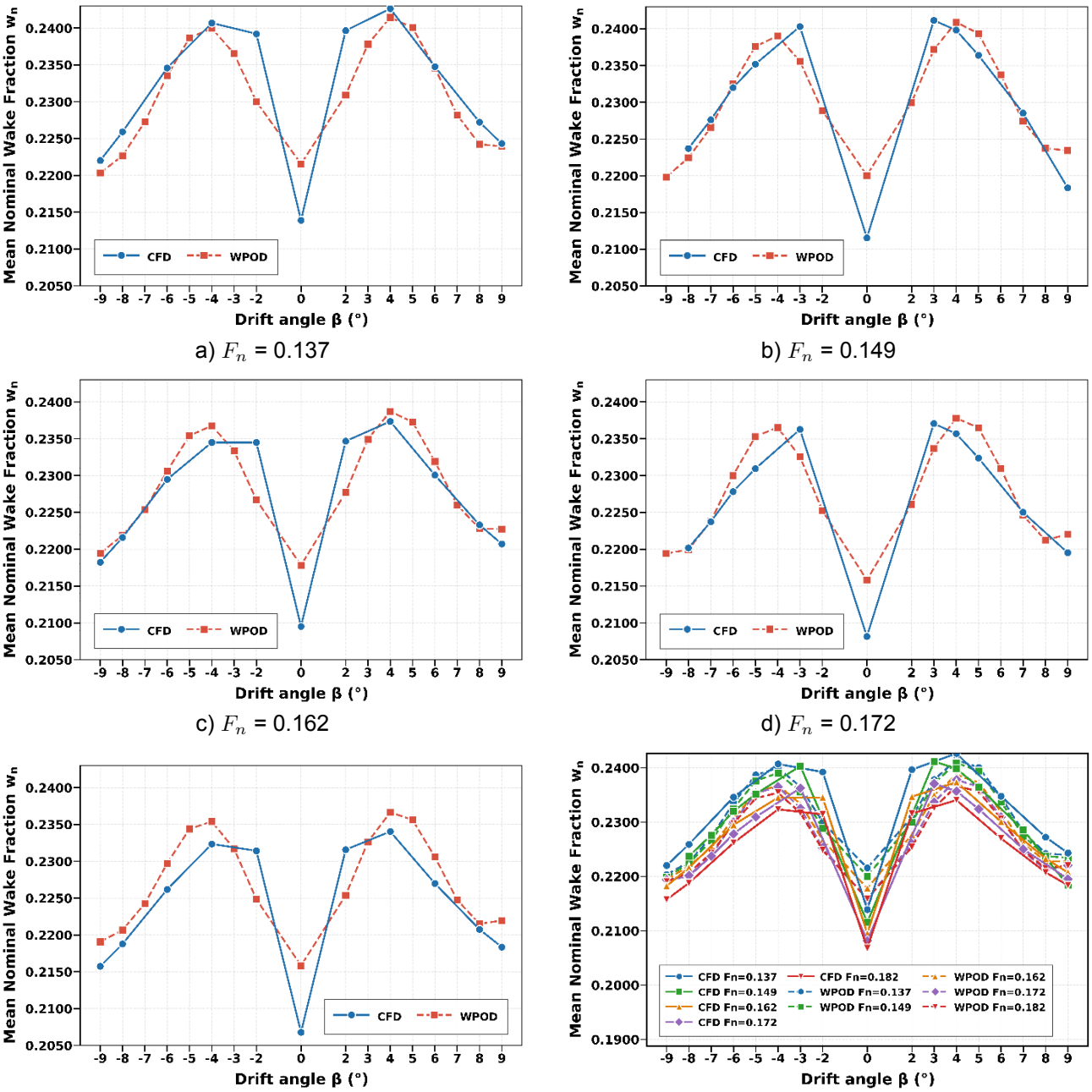


Figure 9. Wake prediction at F_n = 0.172 and drift angle β = −8°: (a) CFD; (b) WPOD; (c) Difference.

Downloaded from onepetro.org/JST/article-pdf/11/01/322/5433561/sname-jst-2026-15.pdf/1 by guest on 03 November 2026



a) F_n = 0.137

b) F_n = 0.149

c) F_n = 0.162

d) F_n = 0.172

e) F_n = 0.182

f) All Froude numbers.

Figure 10. Mean nominal wake fraction: (a) F_n = 0.137; (b) F_n = 0.149; (c) F_n = 0.162; (d) F_n = 0.172; (e) F_n = 0.182; (f) all Froude numbers.

Downloaded from onepetro.org/JST/article-pdf/11/01/322/5433561/sname-jst-2026-15.pdf/1 by guest on 03 November 2026

The pressure coefficient is computed using Equation 15:

$$C_{\mathrm{P}} = \frac{P}{\frac{1}{2}\rho V_{\mathrm{s}}^2}, \tag{15}$$

where P is the total pressure (Pa) and ρ is the water density. As shown in Figure 11, a total of 20 modes are retained to improve the prediction of the pressure distribution. The pressure coefficient used for reconstruction ranges between −1.3 and 1.2. For different drift angles and sail thrust, keeping the pressure as a dimensional value (Pa) becomes challenging due to the large range of values to be predicted. Therefore, the pressure coefficient is used instead to normalize the data and improve the robustness of the model. CFD simulation data corresponding to sail thrust conditions of 0%, 30%, and 50% are used to construct the model. The construction of the model requires approximately 25 s.

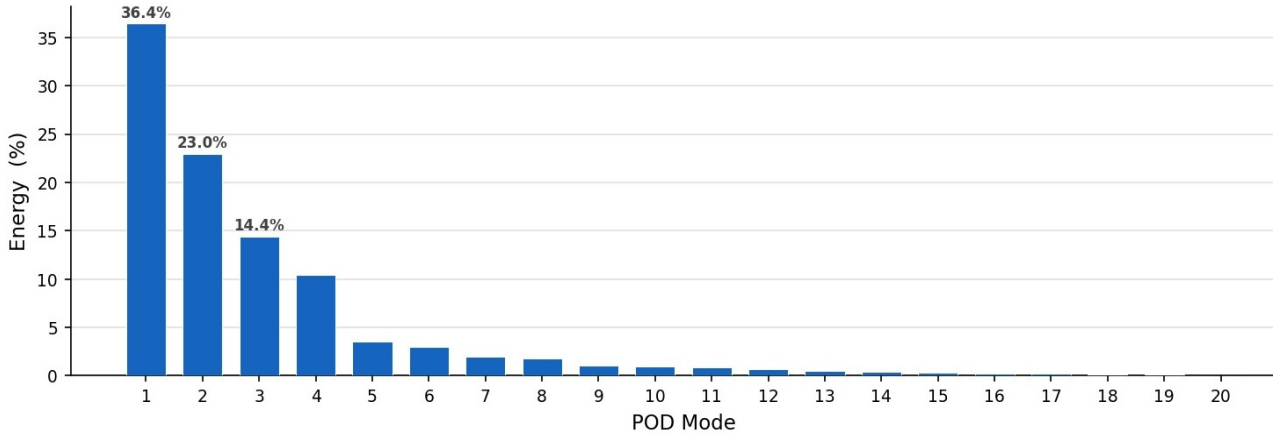


Figure 11. POD mode analysis of pressure coefficient: energy distribution.

Figure 12 and Figure 13 show the pressure distribution obtained from the CFD simulations (target results) and the corresponding predictions from the WPOD model. The difference between the two fields is also presented to assess the discrepancy between the target and predicted pressure distributions. These figures correspond to a sail thrust condition of 10% for drift angles β = 0° and β = 5°. The plots show very close agreement between the CFD and WPOD results, with a local maximum error of about 10% and an area-weighted average error below 6%.

Figure 14 shows the pressure distribution for the 40% sail thrust condition at a drift angle of β = −6°, which was not included in the construction dataset. The local comparison error of the pressure field predicted by POD relative to CFD remains below 10%, with an area-weighted average comparison error of approximately 7%.

With the predicted pressure, the pressure force components are obtained by integrating the pressure over the hull surface. The pressure force coefficients, namely the pressure resistance coefficientC_{rP} and the side pressure force coefficient C_{SP}, are given in Equations 16 and 17.

$$C_{\mathrm{rP}} = \frac{\sum C_{\mathrm{P}} A_i}{S_{\mathrm{w}}}, \tag{16}$$

$$C_{\mathrm{SP}} = \frac{\sum C_{\mathrm{P}} A_j}{S_{\mathrm{w}}}, \tag{17}$$

where A_i and A_j are the projected face areas in the x- and y-directions, respectively, corresponding to each cell face. Figure 15 shows the pressure resistance coefficient at different drift angles for the

Downloaded from onepetro.org/JST/article-pdf/11/01/322/5433561/sname-jst-2026-15.pdf/1 by guest on 03 November 2026

sail thrust conditions of 10% and 20%, and for all sail thrust conditions. The pressure resistance increases with increasing drift angle. The WPOD predictions closely follow the CFD results, with only minor differences. Overall, the predictions match the reference CFD solutions very well, with an average error below 1%. Similarly, the side-pressure force coefficient C_{SP} plots in Figure 16 show very close agreement between the WPOD predictions and the CFD results, with an average prediction error below 1%. This side force does not include the propeller side force.

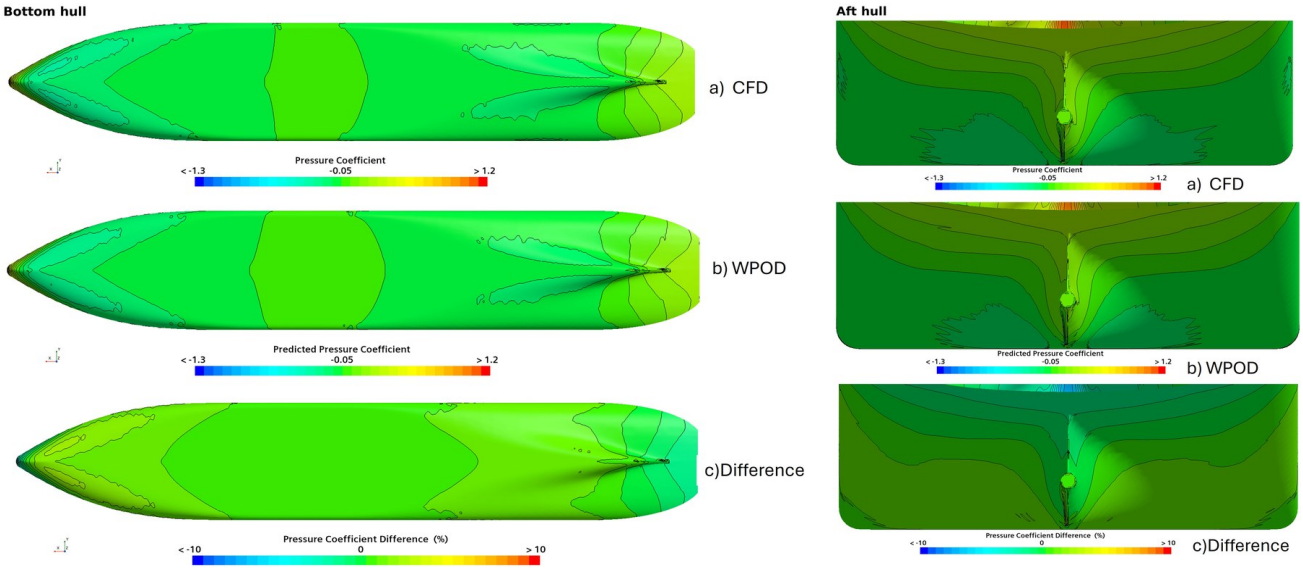


Figure 12. Pressure distribution comparisons for drift angle β = 0° and 10% sail thrust condition: (a) CFD; (b) WPOD; (c) Difference.

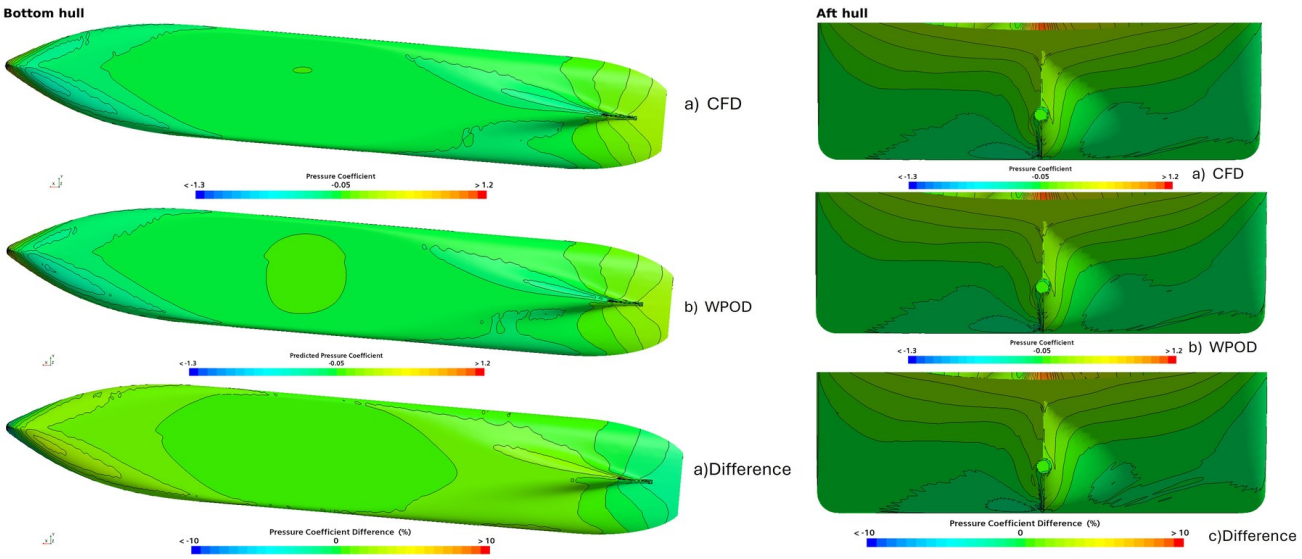


Figure 13. Pressure distribution comparisons for drift angle β = 5° and 10% sail thrust condition: (a) CFD; (b) WPOD; (c) Difference.

Downloaded from onepetro.org/JST/article-pdf/11/01/322/5433561/sname-jst-2026-15.pdf/1 by guest on 03 November 2026

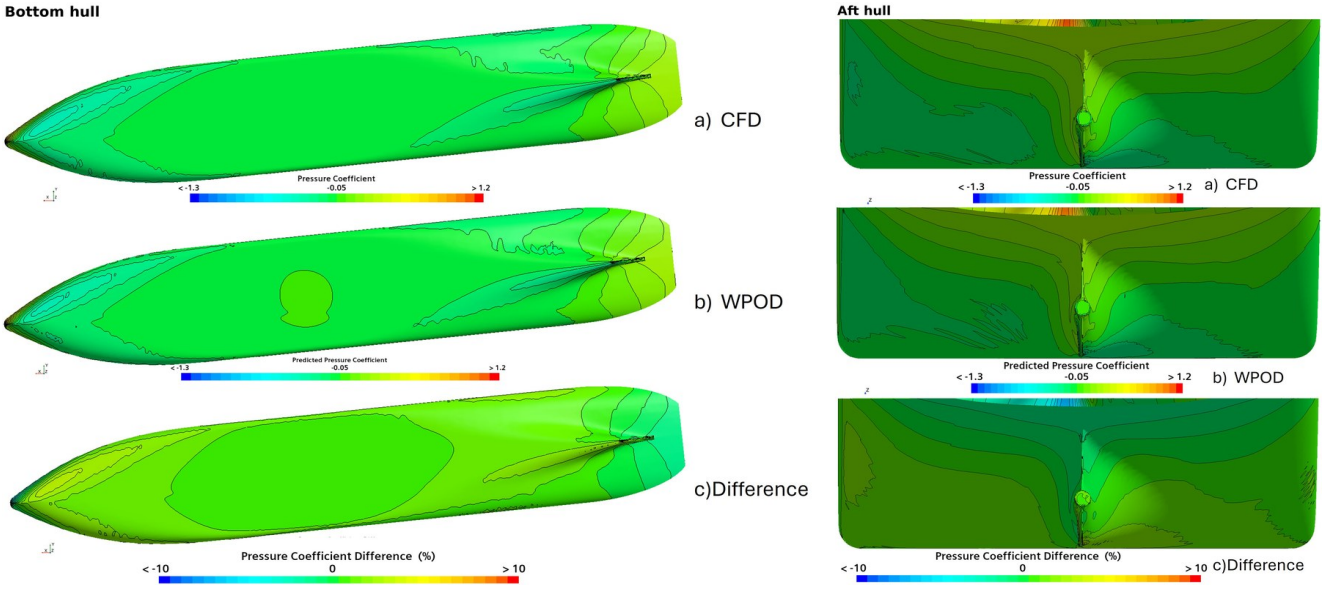


Figure 14. Pressure distribution comparisons for drift angle β = −6° and 40% sail thrust condition: (a) CFD; (b) WPOD; (c) Difference.

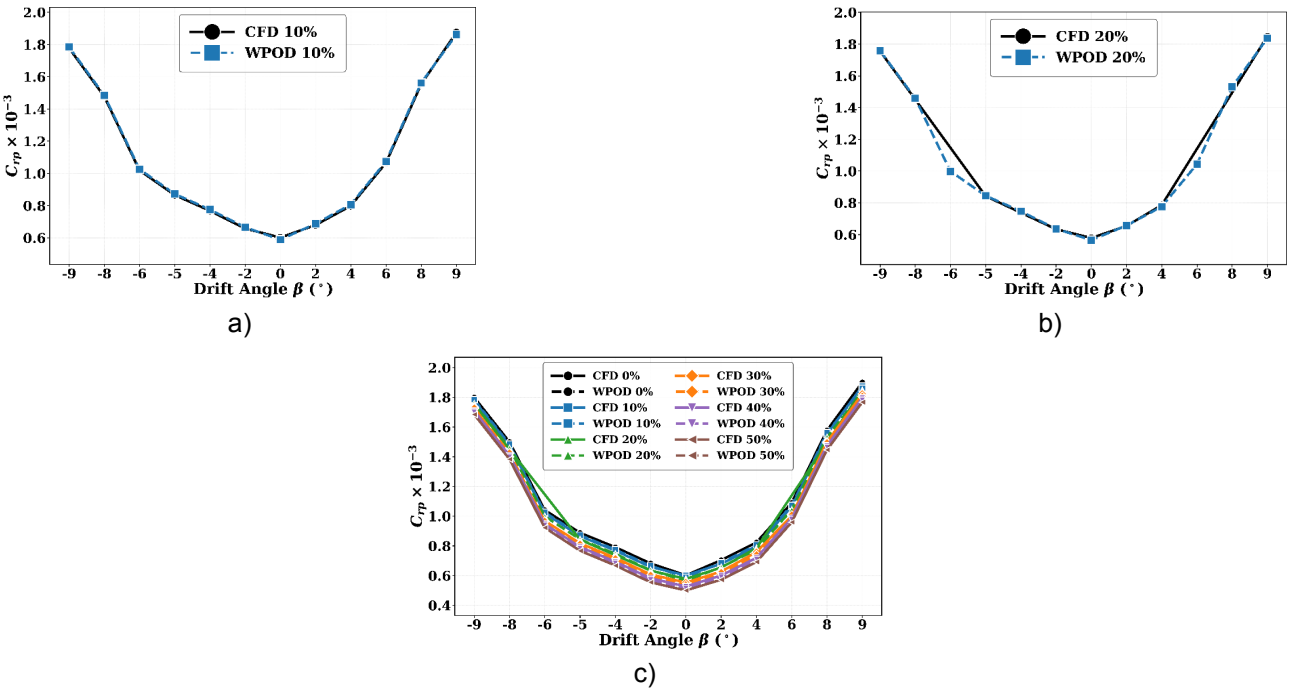


Figure 15. Pressure resistance coefficient C_{rP} obtained from POD and CFD: (a) 10% sail thrust; (b) 20% sail thrust; (c) all sail thrust conditions.

3.4 Skin Friction Prediction

The wall shear stress or skin friction force represents the second component of the forces acting on the hull and plays an important role in evaluating the total force applied to the ship. This subsection analyzes the wall shear stress acting on the hull by comparing the CFD results with those of the bare hull configuration. Similarly to the pressure coefficient analysis, a skin friction coefficient is defined to facilitate the comparison. The skin friction coefficient is computed using Equation 18:

Downloaded from onepetro.org/JST/article-pdf/11/01/322/5433561/sname-jst-2026-15.pdf/1 by guest on 03 November 2026

$$C_\tau = \frac{\tau}{\frac{1}{2}\rho V_s^2}, \tag{18}$$

where τ denotes the wall shear stress (Pa). The accumulation of 20 modes of energy is used to build the POD, as shown in Figure 17.

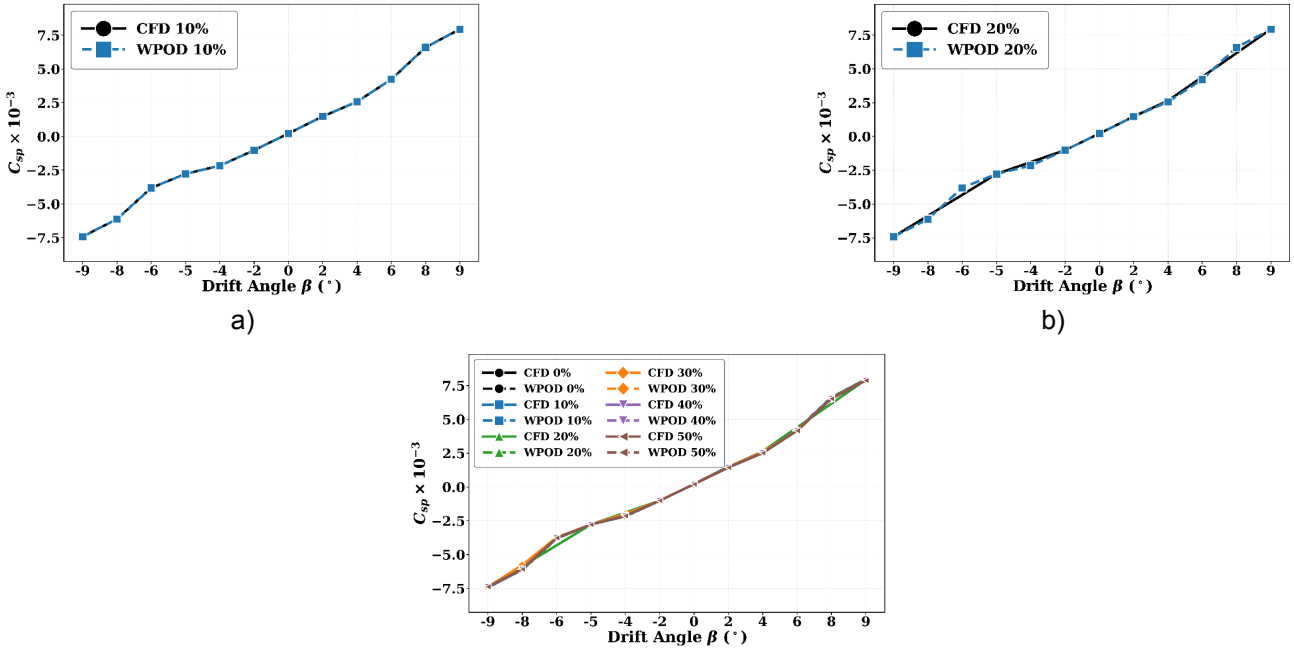


Figure 16. Pressure side force coefficient C_{SP} obtained from POD and CFD: (a) 10% sail thrust; (b) 20% sail thrust; (c) all sail thrust conditions.

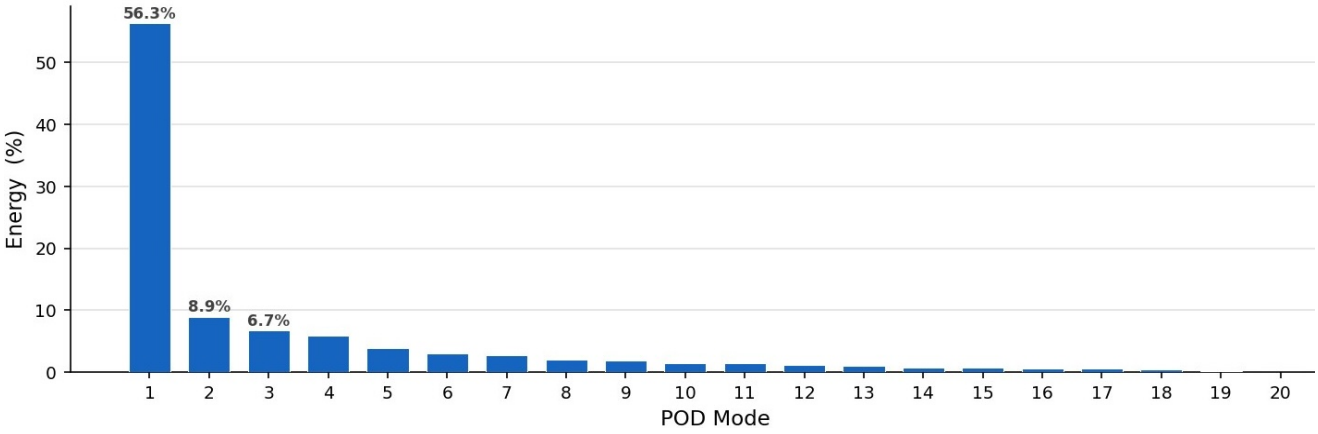


Figure 17. POD mode analysis of wall shear stress coefficient: energy distribution.

Figure 18 and Figure 19 present the wall shear stress distribution on the hull for the 10% sail thrust condition at a drift angle β = 0° and the 40% sail thrust condition at β = −6°, respectively. The wall shear stress distribution predicted by the model closely matches the CFD results. For both cases, the maximum local comparison error remains below 10%, with an area-weighted surface average comparison error of approximately 8%.

Downloaded from onepetro.org/JST/article-pdf/11/01/322/5433561/sname-jst-2026-15.pdf/1 by guest on 03 November 2026

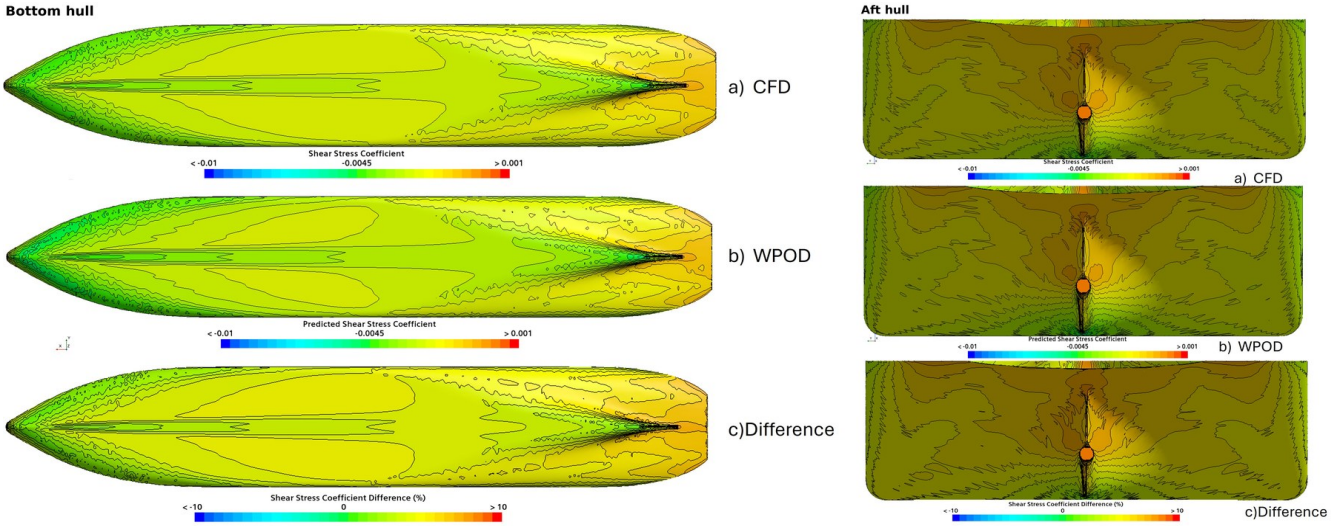


Figure 18. Wall shear stress distribution comparisons for drift angle β = 0° and 10% sail thrust condition: (a) CFD; (b) WPOD; (c) Difference.

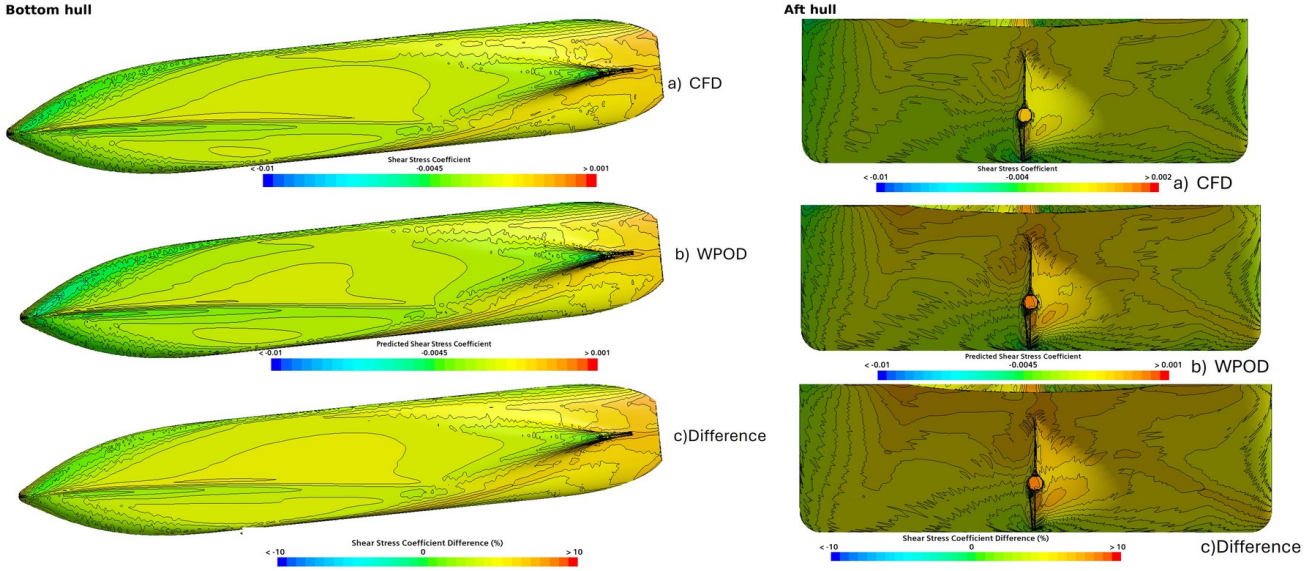


Figure 19. Wall shear stress distribution comparisons for drift angle β = −6° and 40% sail thrust condition: (a) CFD; (b) WPOD; (c) Difference.

The wall shear stress force can be expressed through the frictional force coefficients, namely the longitudinal frictional resistance C_{rf} and the transverse side-friction force C_{sf}. These coefficients are defined in Equations 19 and 20:

$$C_{\mathrm{rf}} = \frac{\sum C_\tau A_i}{S_{\mathrm{w}}}, \tag{19}$$

$$C_{\mathrm{Sf}} = \frac{\sum C_\tau A_j}{S_{\mathrm{w}}}. \tag{20}$$

Figure 20 shows the frictional resistance (wall shear stress) for sail thrust conditions of 10%, 20%, and all sail thrust cases. For the 10% sail thrust case, the maximum difference between the CFD and POD results is about 5%, with an average variation of 3%. The predicted results for the sail thrust cases remain close to each other; however, when compared to CFD data, an average error of approximately 5% is observed. In general, frictional resistance predictions are less accurate than pressure resistance predictions. Nevertheless, the overall agreement remains acceptable. The side

Downloaded from onepetro.org/JST/article-pdf/11/01/322/5433561/sname-jst-2026-15.pdf/1 by guest on 03 November 2026

force predicted using WPOD is compared with CFD results in Figure 21. The predicted side force shows very good agreement with the target results, with better accuracy than the frictional resistance coefficient C_{rf}. The average prediction error is below 1%.

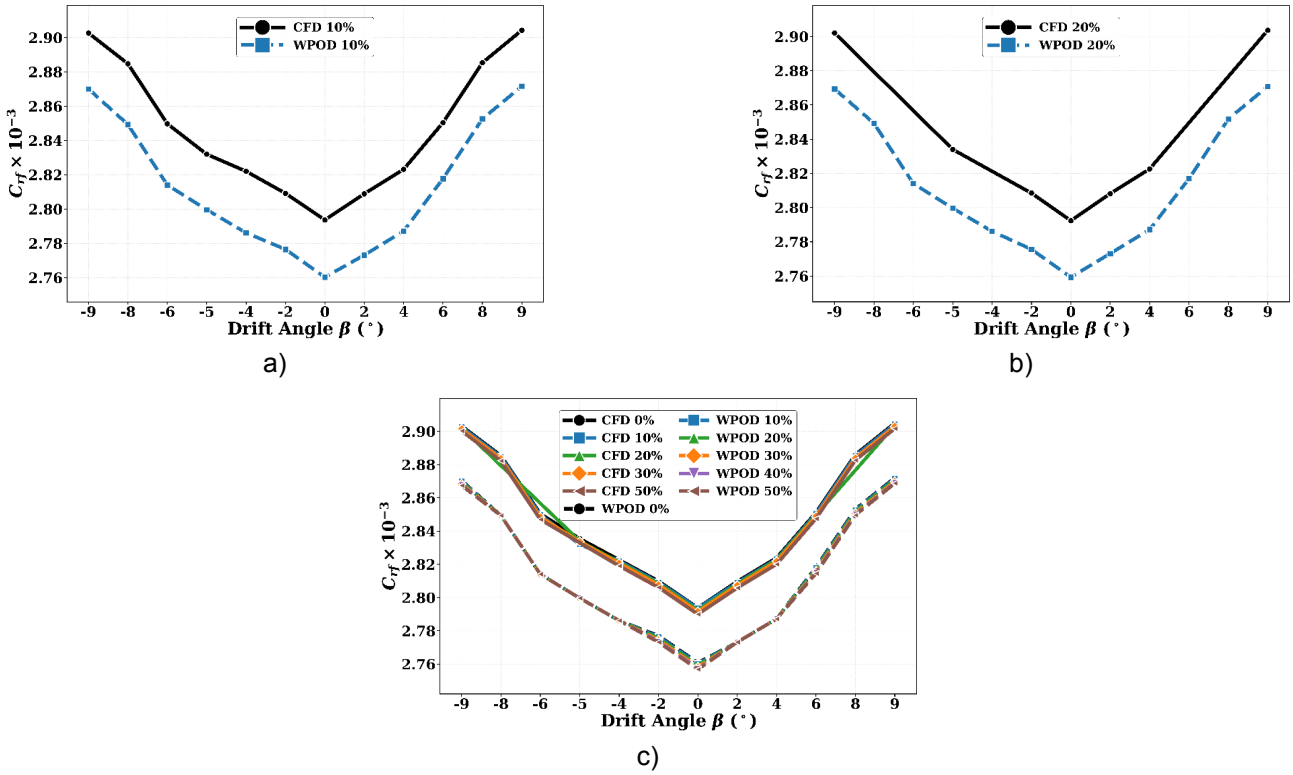


Figure 20. Frictional resistance coefficient C_{rf} obtained from POD and CFD: (a) 10% sail thrust; (b) 20% sail thrust; (c) all sail thrust conditions.

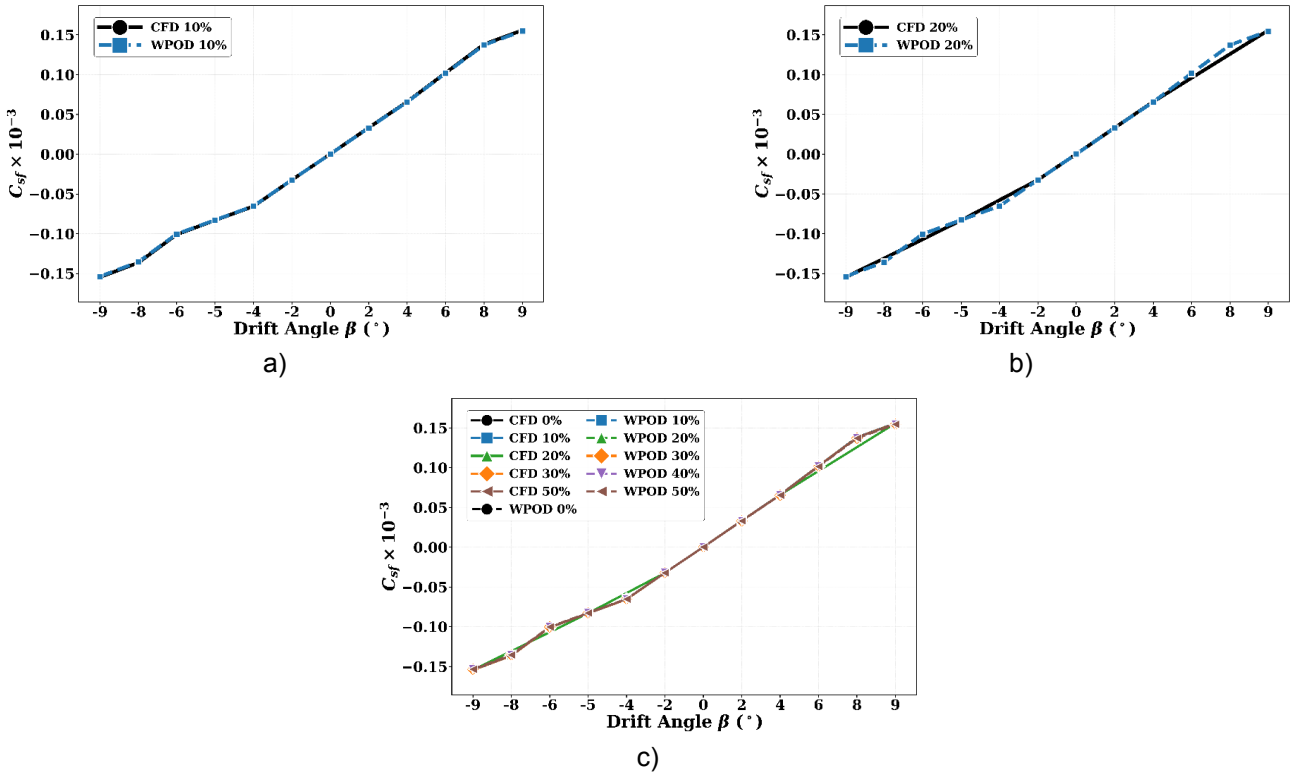


Figure 21. Frictional side force coefficient C_{Sf} obtained from POD and CFD: (a) 10% sail thrust; (b) 20% sail thrust; (c) all sail thrust conditions.

Downloaded from onepetro.org/JST/article-pdf/11/01/322/5433561/sname-jst-2026-15.pdf/1 by guest on 03 November 2026

3.5 Total Resistance

The predicted pressure and wall shear stress components are used to estimate both the total resistance and the side forces acting on the hull. The total resistance is defined as $C_{\mathrm{r}} = C_{\mathrm{rf}} + C_{\mathrm{rP}}$, and the total side force coefficient is defined as $C_{\mathrm{S}} = C_{\mathrm{Sf}} + C_{\mathrm{SP}}$. Figure 22 presents the total resistance C_{r} for different sail thrust conditions. At higher drift angles, the predicted results show good agreement with the CFD data, whereas larger discrepancies are observed at lower drift angles. The average prediction error remains below 4%. Similarly, the total side force coefficient C_{S} in Figure 23 agrees well with CFD results, with an average prediction error of approximately 3%.

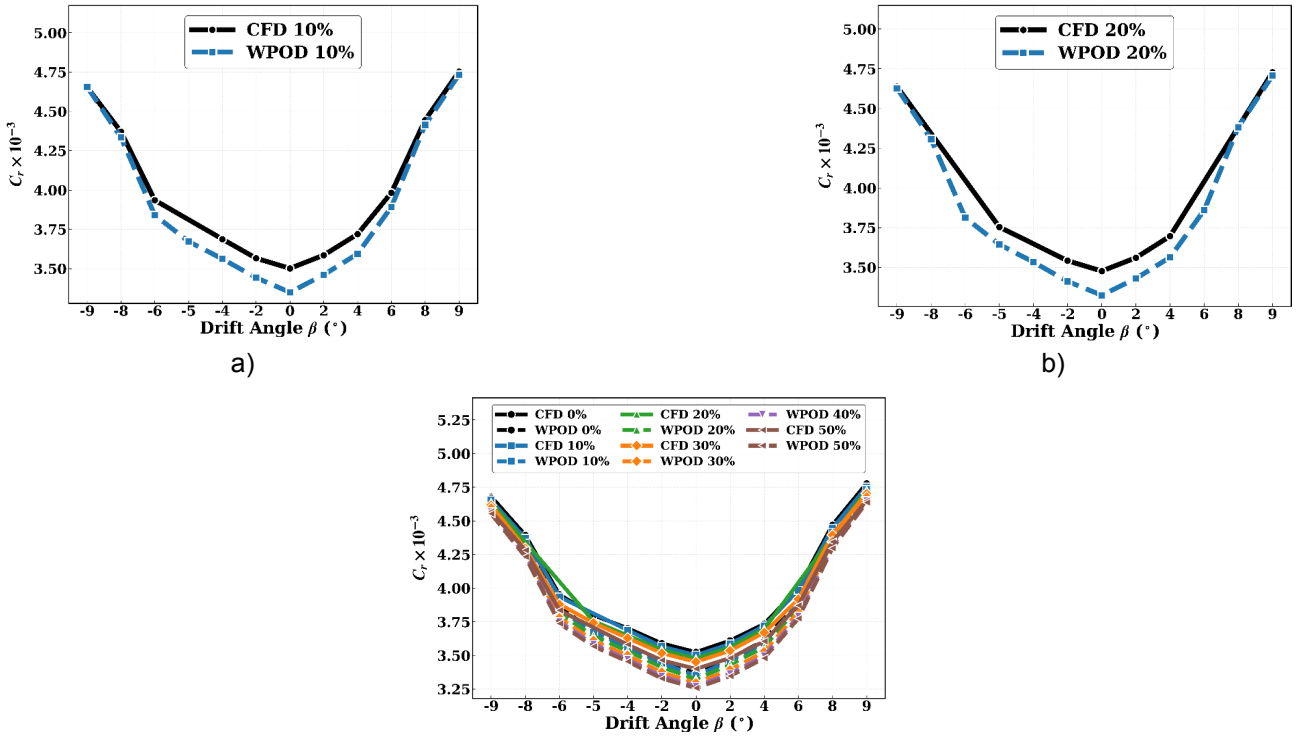


Figure 22. Total resistance coefficient C_{r} obtained from POD and CFD: (a) 10% sail thrust; (b) 20% sail thrust; (c) all sail thrust conditions.

3.6 CFD Uncertainty and ROM Prediction Error

The numerical uncertainty of the CFD simulations has been calculated following the procedure proposed by Eça and Hoekstra (2014), as previously reported in Bakari, A. Malik et al. (2026). According to that study, the numerical uncertainty of the computed resistance of the self-propelled hull is 18%. The numerical uncertainty of the finer grids was found to be considerably lower. However, since the objective of the current study is to assess the performance of the ROM, and not the uncertainty of the CFD computations, the CFD data from the existing grid was used rather than those from the finer grids with smaller uncertainty.

The ROM prediction error, defined as the relative difference between ROM and CFD results, is 2.41% for the mean wake fraction and 3.5% for the total resistance coefficient. Unlike CFD uncertainty, this is a deterministic error, not a probabilistic uncertainty. The ROM provides reliable approximations within the reference CFD simulation accuracy.

Downloaded from onepetro.org/JST/article-pdf/11/01/322/5433561/sname-jst-2026-15.pdf/1 by guest on 03 November 2026

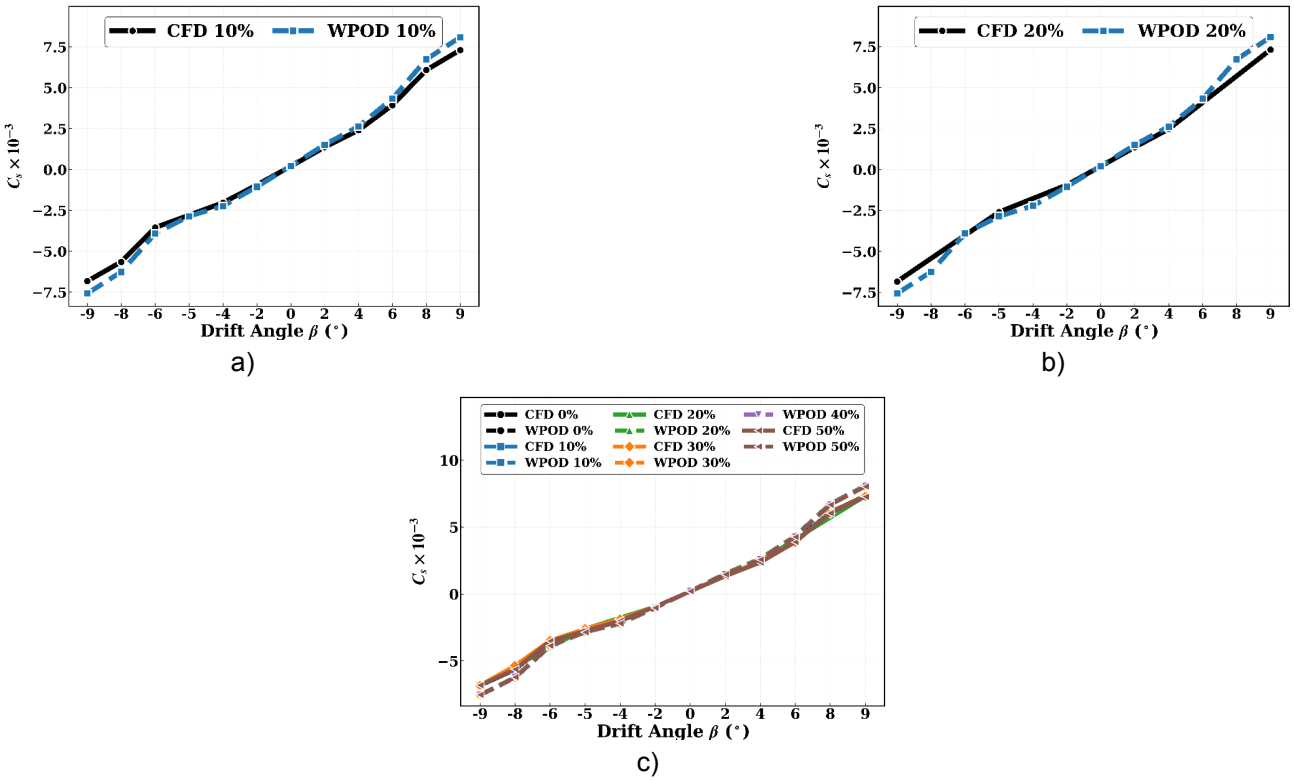


Figure 23. Total side force coefficient C_S obtained from POD and CFD: (a) 10% sail thrust; (b) 20% sail thrust; (c) all sail thrust conditions.

4 COMPUTATION COST

Computational cost is a key aspect of this study. The CFD simulations are divided into two main categories: bare hull simulations and self-propulsion simulations. The bare hull simulations are used to analyze the wake profile at the propeller plane, while the self-propulsion simulations provide the pressure and wall shear stress distributions. In terms of computational effort, each bare hull simulation requires approximately 190 core-hours, whereas each self-propulsion simulation requires about 520 core-hours. For the dataset used to build the WPOD model for construction, bare-hull simulations are performed at 13 drift angles across three different Froude numbers. For validation, 11 drift angles are considered for two additional Froude numbers. Similarly, self-propulsion simulations are conducted at 13 drift angles for each sail thrust condition (0%, 30%, and 50%) in the construction set. For validation, 11 drift angles are used for each sail thrust case (10%, 20%, and 40%). The CFD computation time is shown in Table 4.

Table 4. Summary of computational cost for the CFD simulations.

Simulation type	Cases	Core-hours per case	Total
Construction dataset			
Bare hull (13 drift angles $\times$ 3 Froude numbers)	39	190	7,410
Self-propulsion (11 drift angles $\times$ 3 sail thrust conditions)	33	520	17,160
Validation dataset			
Bare hull (11 drift angles $\times$ 2 Froude numbers)	22	190	4,180
Self-propulsion (11 drift angles $\times$ 3 sail thrust conditions)	33	520	17,160
Total (core-hours)	127		45,910

Downloaded from onepetro.org/JST/article-pdf/11/01/322/5433561/sname-jst-2026-15.pdf/1 by guest on 03 November 2026

Regarding the WPOD approach, three models are constructed: the wake model, the pressure coefficient model, and the wall shear stress coefficient model. The wake model requires approximately 17 s to build, while the pressure and wall shear stress models each require about 20 s. Once trained, the prediction of a single case takes approximately 1 s. For the wake model, generating all results for 5 Froude numbers and 17 drift angles requires about 85 s. Similarly, for both the pressure and wall shear stress models, covering 5 sail thrust conditions and 17 drift angles also require approximately 85 s each as presented in the Table 5.

Table 5. Summary of computational time for the WPOD models.

WPOD Model	Model construction time (s)	Number of cases	Result generation (s)
Wake	17	85 (5 F_n $\times$ 17β)	85
Pressure	20	85 (5 sail thrust $\times$ 17β)	85
Wall shear stress	20	85 (5 sail thrust $\times$ 17β)	85
Total	**57**	**255**	**255**

5 CONCLUSIONS

In this study, a hybrid method combining WPOD and Kriging interpolation is employed to develop a Reduced-Order Model to predict the nominal wake fraction, pressure distribution, and wall shear stress for a WASP. The JoRes1 tanker is used as the test case to analyze nominal wake-fraction variations in bare-hull simulations for different drift angles and Froude numbers, as well as changes in pressure and wall shear stress around the hull under self-propulsion conditions, using a virtual disk method and considering different sail thrust conditions and drift angles. The study is divided into three main parts.

The first part focuses on predicting the wake field using data obtained from CFD simulations. The constructed WPOD model is used to predict new wake fields, from which the mean wake fraction is computed and compared with CFD results. The area-weighted surface average comparison error of the predicted wake field remains below 10%, while the mean wake prediction achieves an average error of 2.41% in comparison to the value obtained from CFD. In the second part, a pressure prediction model is developed using self-propulsion results from CFD simulations. The pressure field is predicted for various sail-thrust contributions and compared with CFD reference data. The pressure distributions are subsequently integrated over the hull surface to compute the pressure force coefficients. The prediction error for these coefficients remains below 1%. The last part extends the methodology to predict wall shear stress distribution. Integration of the predicted wall shear stress yields the frictional force coefficients, with an average prediction error of approximately 5% in comparison to the value obtained from CFD. The pressure and wall shear stress forces are then combined to calculate the total resistance, achieving high prediction accuracy with an average error of 3.5% relative to the reference CFD simulation.

Overall, the WPOD-Kriging method demonstrates high accuracy while requiring only 5 minutes and 12 seconds for all predictions, which is negligible compared to the cost of a new CFD simulation. For WASP applications involving multiple parameters such as Froude number, sail thrust, and drift angle, CFD simulations become expensive. The WPOD-Kriging model provides an efficient and reliable alternative for rapid prediction of hydrodynamic performance.

ACKNOWLEDGEMENTS

This work was financially supported by the Swedish Transport Agency. Computational resources were provided by the National Academic Infrastructure for Supercomputing in Sweden (NAISS) under

Downloaded from onepetro.org/JST/article-pdf/11/01/322/5433561/sname-jst-2026-15.pdf/1 by guest on 03 November 2026

projects Naiss2025-5-609 and Naiss2025-5-67, as well as by the Chalmers Centre for Computational Science and Engineering (C3SE) under project C3SE2026-1-1.

REFERENCES

Ammar, N. R. and Seddiek, I. S. (2022). Wind Assisted Propulsion System Onboard Ships: Case Study Flettner Rotors. *Ships and Offshore Structures* 17.7, pp. 1616–1627. ISSN: 1744-5302. DOI: 10.1080/17445302.2021.1937797.

Bakari, A. Malik, Bensow, Rickard, Lopes, Rui, and Eslamdoost, Arash (2025). Toward Obtaining the Propulsive Factors for a Wind-Assisted Ship. *Proceedings of the 27th Numerical Towing Tank Symposium (NuTTS).* Zagreb, Croatia, pp. 14–19.

Bakari, A. Malik, Lopes, Rui, Shiri, and Eslamdoost, Arash (2026). Thrust Deduction Analysis for Wind-Assisted Ships. *Proceedings of the Ninth International Symposium on Marine Propulsors (SMP'26).* St. John's, Canada.

Bickert, F., Gentaz, L., and Babarit, A. (2026). Effect of Wind Propulsion Systems on Sail-Induced Resistance, Rudder Angle and Heel Angle for the KVLCC2 and the KCS Vessels. *Journal of Sailing Technology* 11.01, pp. 1–30. ISSN: 2475-370X. DOI: 10.5957/jst/2026.11.1.1.

Clayton, B. R. (1987). Wind-Assisted Ship Propulsion. *Physics in Technology* 18.2, p. 53. ISSN: 0305-4624. DOI: 10.1088/0305-4624/18/2/301.

Eça, L. and Hoekstra, M. (2014). A Procedure for the Estimation of the Numerical Uncertainty of CFD Calculations Based on Grid Refinement Studies. *Journal of Computational Physics* 262, pp. 104–130. ISSN: 00219991. DOI: 10.1016/j.jcp.2014.01.006.

Giere, S. (2016). Numerical and Analytical Aspects of Pod-Based Reduced-Order Modeling in Computational Fluid Dynamics. PhD thesis. URL: https://refubium.fu-berlin.de/handle/fub188/13554 (visited on 08/08/2026).

HSVA (2023). *Model Tests for JoRes Tanker 1*. RP-2023-033. Hamburg Germany.

Huayamave, V., Ceballos, A., Barriento, C., Seigneur, H., Barkaszi, S., Divo, E., and Kassab, A. (2017). RBF-Trained POD-accelerated CFD Analysis of Wind Loads on PV Systems. *International Journal of Numerical Methods for Heat & Fluid Flow* 27.3, pp. 660–673. ISSN: 0961-5539. DOI: 10.1108/HFF-03-2016-0083.

IMO (2023). *IMO Strategy on Reduction of GHG Emissions from Ships. Resolution MEPC. 377 (80)*.

ITTC (2011). *Recommended Procedures and Guidelines: Practical Guidelines for Ship CFD Applications.* 7.5–03–02–03.

Jiang, L., Yao, J., and Liu, Z. (2022). Comparison Between the RANS Simulations of Double-Body Flow and Water–Air Flow Around a Ship in Static Drift and Circle Motions. *Journal of Marine Science and Engineering* 10.7, p. 970. ISSN: 2077-1312. DOI: 10.3390/jmse10070970.

JoRes Project (2023). *Ship Scale Validation Cases for Energy Efficiency Solutions.* URL: https://jores.net/.

Khan, L., Macklin, J. J. R., Peck, B. C. D., Morton, O., and Souppez, J.-B. R. G. (2021). A Review Of Wind-Assisted Ship Propulsion For Sustainable Commercial Shipping: Latest Developments And Future Stakes. *Wind Propulsion 2021*. DOI: 10.3940/rina.win.2021.05.

Downloaded from onepetro.org/JST/article-pdf/11/01/322/5433561/sname-jst-2026-15.pdf/1 by guest on 03 November 2026

Kolda, T. G. (2003). A Counterexample to the Possibility of an Extension of the Eckart--Young Low-Rank Approximation Theorem for the Orthogonal Rank Tensor Decomposition. *SIAM Journal on Matrix Analysis and Applications* 24.3, pp. 762–767. ISSN: 0895-4798, 1095-7162. DOI: 10.1137/S0895479801394465.

Larsson, L., Stern, F., and Visonneau, M. (2013). CFD in Ship Hydrodynamics—Results of the Gothenburg 2010 Workshop. *MARINE 2011, IV International Conference on Computational Methods in Marine Engineering*. Ed. by L. Eça, E. Oñate, J. García-Espinosa, T. Kvamsdal, and P. Bergan. Computational Methods in Applied Sciences. Dordrecht: Springer Netherlands, pp. 237–259. ISBN: 978-94-007-6142-1. DOI: 10.1007/978-94-007-6143-8_14.

Lindstad, E., Stokke, T., Alteskjær, A., Borgen, H., and Sandaas, I. (2022). Ship of the Future – A Slender Dry-Bulker with Wind Assisted Propulsion. *Maritime Transport Research* 3, p. 100055. ISSN: 2666822X. DOI: 10.1016/j.martra.2022.100055.

Lu, R. and Ringsberg, J. W. (2020). Ship Energy Performance Study of Three Wind-Assisted Ship Propulsion Technologies Including a Parametric Study of the Flettner Rotor Technology. *Ships and Offshore Structures* 15.3, pp. 249–258. ISSN: 1744-5302. DOI: 10.1080/17445302.2019.1612544.

Mohammadi, A. and Raisee, M. (2019). Stochastic Field Representation Using Bi-Fidelity Combination of Proper Orthogonal Decomposition and Kriging. *Computer Methods in Applied Mechanics and Engineering* 357, p. 112589.

Ortali, G., Demo, N., and Rozza, G. (2021). A Gaussian Process Regression Approach Within a Data-Driven POD Framework for Engineering Problems in Fluid Dynamics. *Mathematics in Engineering* 4, pp. 1–16. DOI: 10.3934/mine.2022021.

Sauder, T. and Alterskjær, S. A. (2022). Hydrodynamic Testing of Wind-Assisted Cargo Ships Using a Cyber–Physical Method. *Ocean Engineering* 243, p. 110206. ISSN: 00298018. DOI: 10.1016/j.oceaneng.2021.110206.

Saydam, A., Küçüksu, G., İnsel, M., and Gökçay, S. (2022). Investigation of the Influence of Wind-Assisted Propulsion Devices on Hull Design. *Sustainable Development and Innovations in Marine Technologies*. 1st ed. London: CRC Press, pp. 211–216. ISBN: 978-1-003-35896-1. DOI: 10.1201/9781003358961-27.

Tang, Y.-Q., Fang, W.-Z., Zheng, C.-Y., and Tao, W.-Q. (2025). Applications of POD-based Reduced Order Model to the Rapid Prediction of Velocity and Temperature in Data Centers. *Applied Thermal Engineering* 263, p. 125310. ISSN: 13594311. DOI: 10.1016/j.applthermaleng.2024.125310.

Van Der Kolk, N., Akkerman, I., Keuning, J., and Huijsmans, R. (2020). Part 2: Simulation Methodology and Numerical Uncertainty for RANS-CFD for the Hydrodynamics of Wind-Assisted Ships Operating at Leeway Angles. *Ocean Engineering* 201, p. 107024. ISSN: 00298018. DOI: 10.1016/j.oceaneng.2020.107024.

Van Der Kolk, N., Keuning, J., and Huijsmans, R. (2019). Part 1: Experimental Validation of a RANS-CFD Methodology for the Hydrodynamics of Wind-Assisted Ships Operating at Leeway Angles. *Ocean Engineering* 178, pp. 375–387. ISSN: 00298018. DOI: 10.1016/j.oceaneng.2018.12.041.

Xia, Z. and Wu, Y. (2025). A WPOD-Kriging Reduced-Order Method for Parametric CFD Simulations. *International Journal for Numerical Methods in Fluids* 97.6, pp. 985–995. ISSN: 1097-0363. DOI: 10.1002/fld.5383.

Downloaded from onepetro.org/JST/article-pdf/11/01/322/5433561/sname-jst-2026-15.pdf/1 by guest on 03 November 2026